

NASA
TN
D-7649
c.1(R)

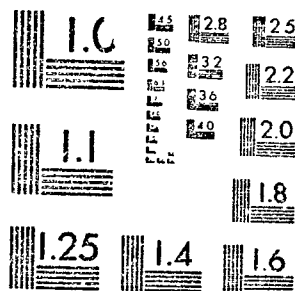
LOAN COPY: RETURN TO AFWL
TECHNICAL LIBRARY, KIRTLAND AFB, NM

1 OF 1

0133578

TECH LIBRARY KAFB, NM

N74-31760 UNCLAS



MICROCOPY RESOLUTION TEST CHART
NATIONAL BUREAU OF STANDARDS-1963-A



0133578

NASA TECHNICAL NOTE



NASA TN D-7649

NASA TN D-7649

(NASA-TN-D-7649) INTERFERENCE HEATING
FROM INTERACTIONS OF SHOCK WAVES WITH
TURBULENT BOUNDARY LAYERS AT MACH 6
(NASA) 73 p HC \$3.75

CSCL 20D

N74-31760

H1/12

Unclass

47483

P 130

INTERFERENCE HEATING FROM
INTERACTIONS OF SHOCK WAVES WITH
TURBULENT BOUNDARY LAYERS AT MACH 6

by Charles B. Johnson and Louis G. Kaufman II

Langley Research Center

Hampton, Va. 23665



NATIONAL AERONAUTICS AND SPACE ADMINISTRATION • WASHINGTON, D. C. • SEPTEMBER 1974

INTERFERENCE HEATING FROM INTERACTIONS OF SHOCK WAVES WITH TURBULENT BOUNDARY LAYERS AT MACH 6*

By Charles B. Johnson and Louis G. Kaufman II**
Langley Research Center

SUMMARY

This paper presents results of an experimental investigation of interference heating resulting from interactions of shock waves and turbulent boundary layers. Pressure and heat-transfer distributions were measured on a flat plate in the free stream and on the wall of the test section of the Langley Mach 6 high Reynolds number tunnel for Reynolds numbers ranging from 2×10^6 to 400×10^6 . Various incident shock strengths were obtained by varying a wedge-shock generator angle (from 10° to 15°) and by placing a spherical-shock generator at different vertical positions above the instrumented flat plate and tunnel wall.

The largest heating-rate amplification factors obtained for completely turbulent boundary layers were 22.1 for the flat plate and 11.6 for the tunnel wall experiments. Maximum heating correlated with peak pressures using a power law with a 0.85 exponent. Measured pressure distributions were compared with those calculated using turbulent free-interaction pressure rise theories, and separation lengths were compared with values calculated by using different methods.

INTRODUCTION

In hypersonic flight, the generation of shock waves by various surfaces of a vehicle or engine and the impingement of those shocks on other surfaces can greatly amplify the local heat transfer and pressure loads on the surfaces. The adverse pressure gradient associated with the impinging shock wave, if sufficiently strong, causes the boundary-layer flow to separate from the surface. There results a region of reverse flow that terminates where the separated boundary layer reattaches to the surface, with attendant high heating rates. The importance of being able to predict when boundary-layer separation occurs, the geometric features of the shock—boundary-layer interaction region,

*This work was initiated jointly by NASA Marshall Space Flight and Langley Research Centers.

**Staff Scientist, Research Department, Grumman Aerospace Corporation; work performed under Langley/Industry Research Associate Program.

and the local heating rates is well recognized and has received much attention. (See refs. 1 and 2.) However, there are still no adequate analytical methods for predicting the extent of separation and the increased heating. (See refs. 3 and 4.) Most of the current approaches to the problem of predicting the characteristics of the shock—boundary-layer interaction region, particularly for turbulent boundary layers, are empirical and are based on data obtained from experiments conducted over relatively limited ranges of test conditions.

Considerable experimental effort has been expended in studying separated flows in a shock—boundary-layer interaction region, a great deal of attention being given to developing a method of predicting incipient separation. (See refs. 5 to 12.) Other characteristics of separated flows that have been investigated are the extent of the separated flow region, the pressure distribution on the surface, and the heat-transfer distribution.

The extent of separation has been shown experimentally (refs. 13 and 14) to scale with boundary-layer thickness and increases with shock strength. Earlier work, based on limited range of test conditions (model length Reynolds numbers less than 6×10^6), indicated that the extent of turbulent boundary-layer separation increased slightly with Reynolds number. (See refs. 13 to 16.) However, Law's (ref. 6) recent work for larger Reynolds numbers indicates a decrease in separation length with increasing Reynolds number. The surface pressure rise up to separation can be estimated by assuming a "free interaction." (See refs. 17 and 18.) The pressure rise downstream of the separation point depends on the impinging shock strength and length of separation. (See ref. 19.) If the pressure distribution is known, then boundary-layer-type analyses can be used to estimate the distribution of heating rates. (See ref. 3.) However, as noted by Gerhart (ref. 3), the boundary-layer analyses fail at the reattachment point. In the immediate vicinity of reattachment, the separated shear layer impinges on the surface, similar to a jet impingement type flow, and the heating is most severe. Many simple correlations (refs. 15 and 20 to 27) have been sought relating the observed peak heating rates and peak pressure values at reattachment. Unfortunately, these correlations are based on data obtained for Reynolds numbers considerably smaller (less than 10×10^6) than those expected for high-speed flight vehicles (greater than 50×10^6).

Relatively few experiments have been conducted for very high Reynolds numbers (refs. 6, 7, 12, and 28), and these investigations have been directed primarily to obtaining incipient separation conditions rather than heat-transfer data. The present investigation was designed to provide surface pressure and heating-rate distributions resulting from incident shock wave impingements for both moderate and very high Reynolds numbers. Therefore, an important objective of the investigation was to enlarge substantially the base for the empirical methods by providing interaction data for a wider range of test conditions, and, in particular, to obtain data for Reynolds numbers comparable to those

expected for flight vehicles. By using both a flat plate in the free-stream flow and an instrumented portion of the tunnel wall, interaction data were obtained for running length Reynolds numbers from 2×10^6 to 400×10^6 for unit Reynolds numbers from 9×10^6 to 120×10^6 per meter. The data were used to improve correlations of separation length and peak heating rates and to determine scaling effects on the correlations. The experiments were conducted in the Langley Mach 6 high Reynolds number tunnel.

SYMBOLS

a_s	height of sphere-cylinder above plate (fig. 2), m
\hat{a}_s	height of sphere-cylinder above tunnel wall (fig. 2), m
a_w	height of wedge leading edge above plate (fig. 2), m
\hat{a}_w	height of wedge leading edge above tunnel wall (fig. 2), m
$c_{f,o}$	coefficient of friction of boundary layer on tunnel wall at $\hat{x} = \hat{x}_o$
c_m	specific heat of model material (stainless steel), J/kg-K
c_p	specific heat of free-stream flow, J/kg-K
F	similarity function used in free-interaction pressure rise (see eq. (8))
$f(P)$	Prandtl-Meyer function of pressure ratio in terms of turning angle $\Delta\nu$
$f_1(p_{pk}, p_{pl})$	function of p_{pk} and p_{pl} defined in equation (10)
$f_2(p_{pk}, p_{pl})$	function of p_{pk} and p_{pl} defined in equation (11)
H	ratio of disturbed to undisturbed heat-transfer coefficients at same location on plate or tunnel wall
h	heat-transfer coefficient, W/K-m ²
k	thermal conductivity, J/sec-m-K
l_{sep}	extent of separated flow upstream of inviscid, incident shock location, m

M	Mach number
N_{Pr}	Prandtl number
N_{St}	Stanton number based on undisturbed flow conditions
n	exponent in peak heating-pressure correlation power law
P	pressure ratio, $\frac{(p/p_\infty)_{\text{disturbed}}}{(p/p_\infty)_{\text{undisturbed}}}$
p	pressure, N/m ²
q	heat-transfer rate, W/m ²
R	unit Reynolds number of free-stream flow, per meter
Re_x	Reynolds number based on free-stream conditions and distance x
$Re_{\hat{x}}$	Reynolds number based on free-stream conditions and distance \hat{x}
$Re_{x,s}$	Reynolds number based on free-stream conditions and distance x_s
$Re_{\hat{x},s}$	Reynolds number based on free-stream conditions and distance \hat{x}_s
r	recovery factor
s	free-interaction pressure rise length coordinate, $\frac{\hat{x} - \hat{x}_0}{\hat{x}_f - \hat{x}_0}$
T	temperature, K
t	time, sec
V	velocity, m/sec
x	streamwise distance from plate leading edge, m
\hat{x}	distance measured along tunnel wall surface from tunnel throat, m
x_f	reference location

x_E	incident shock location on plate, calculated inviscidly, m
\hat{x}_S	incident shock location on tunnel wall, calculated inviscidly, m
z	distance normal to the model surface, m
γ	ratio of specific heats (taken as 1.4 herein)
$\Delta\nu$	change in Prandtl-Meyer turning angle, deg
δ	boundary-layer thickness, m
δ_S	thickness of free-stream layer
θ_w	wedge shock generator angle, deg
μ	viscosity of flow, N-sec/m ²
ρ	density of flow, kg/m ³
ρ_m	density of model material (stainless steel), kg/m ³
τ_m	thickness of heat-transfer-model wall
ϕ	flow deflection angle at reattachment, deg

Subscripts:

aw	adiabatic wall conditions
e	conditions at outer edge of boundary layer
o	undisturbed conditions immediately upstream of interaction effects
pk	peak (maximum) conditions
pl	plateau conditions
r	conditions downstream of reattachment

t	total (stagnation) conditions
w	wall conditions
1	undisturbed flow conditions
∞	free-stream conditions

APPARATUS AND TEST PROCEDURES

Test Facility

The experiments were conducted in the Langley Mach 6 high Reynolds number tunnel. This is a closed circular test section, 30.48 cm in diameter, a blowdown wind tunnel that can provide Mach 6 free-stream flows for unit Reynolds numbers varying from 5×10^6 to 140×10^6 per meter. (See ref. 29.)

The tunnel has a model injection system directly beneath the test section (shown in fig. 1). Although full injection from the bottom of the vacuum tight chamber to tunnel center line requires 1 second, the model passes through the tunnel wall shear layer in less than 0.2 second.

Models

In order to provide incident shock data for both moderate and high Reynolds numbers, two types of shock receivers were used. Moderate Reynolds numbers were obtained on a flat-plate shock receiver mounted in the tunnel free stream. Very high Reynolds numbers were achieved by using an instrumented portion of the curved tunnel wall as the shock receiver.

Wedges and spheres were used to generate the shock waves that impinged either on the instrumented flat plate or on the instrumented portion of the tunnel wall. For all tests, the shock generators were sting mounted to vertical struts. For the "free-stream" experiments, the instrumented flat plate was cantilevered forward from the same strut (fig. 2).

The wedge shock generator could be set at 10° , 12.5° , or 15° angles (θ), which were sufficient to cause moderate extents of separated flow. Smaller wedge angles would have resulted in shock strengths insufficient to separate the turbulent boundary-layer flows. Larger angles would have resulted in extensive separation and would have introduced extraneous effects influencing the flow in the reattachment region, such as reflected compression waves and/or the expansion wave from the wedge trailing edge

coalescing in the reattachment region. Thus, the attempt was made to provide as large a region of "clean" shock impingement interaction flow as possible, without choking the tunnel flow.

As indicated in figure 2, the wedge generator was 19.05 cm long and had a span of 15.24 cm. The sphere-cylinder shock generator had an overall length of 5.40 cm and a diameter of 5.08 cm. Both the wedge and sphere could be set at various streamwise stations and at various heights above the shock receivers. The heights are taken in the tunnel center plane and are referenced either to the wedge leading edge or to the lower surface of the sphere-cylinder. The streamwise stations are referenced to the locations where the generator shock waves impinge on the plate surface (x_s). The distance \hat{x}_s is measured along the tunnel wall surface from the throat of the tunnel.

Instrumentation

Two (interchangeable) flat-plate shock receivers were used, one instrumented with 48 thermocouples along the plate center line, and one with pressure orifices at the same locations. As indicated in figure 3(a), the plates had chords of 45.60 cm and spans of 17.46 cm. The first instrumentation location was 13.94 cm downstream of the leading edge, and the thermocouples and pressure orifices were evenly spaced 0.508 cm apart. The iron/constantan thermocouples were spotwelded to the inner surface of a "thin skin" section of the heat-transfer plate. The skin thickness in this region was 0.076 cm. The pressure plate had a constant wall thickness of 0.318 cm.

Similarly, two interchangeable tunnel wall sections were used. As indicated in figure 3(b), these cylindrical plates were sealed and flush with the tunnel wall. Again, 48 thermocouples or 48 pressure orifices were evenly spaced (0.508 cm apart) along the plate center lines. The first instrumentation location was 3.068 m downstream of the tunnel throat (measured along the tunnel wall surface). The heat-transfer plate had a thin wall in the region of the thermocouples (0.076 cm thick), and overall dimensions of 107.63 cm by 17.46 cm. The radius of curvature of the inner wall was 15.24 cm to conform to the circular test section of the tunnel. The curved pressure plate had the same overall dimensions and a wall thickness of 0.318 cm.

Test Conditions

The experiments were conducted at five nominal tunnel stagnation pressure levels given in table I. Nominal total temperatures and unit Reynolds numbers (per meter) are also shown. The corresponding Reynolds numbers based on distance measured along the flat-plate surface varied from 1.4×10^6 to 40×10^6 . The Reynolds numbers based on distance measured along the tunnel wall from the tunnel throat to the instrumented curved plate varied from 20×10^6 to 440×10^6 .

Heat-transfer data were obtained for several shock generator locations over the full range of test conditions. Pressure data were obtained only for selected shock generator locations.

Test Procedures and Data Reduction

For both the pressure and heat-transfer experiments, the tunnel flow was first started and established, the model injected into the tunnel flow, data recorded, and then the model was retracted prior to stopping the tunnel flow. Pressures were recorded by using standard mercury manometer boards. Heat-transfer data were obtained using thermocouples and the thin-wall transient-temperature technique. Schlieren flow photographs were taken during each tunnel run, although in most instances the shock-wave—boundary-layer interaction region was outside the tunnel window field of vision.

The manometers were observed to stabilize within 10 to 15 seconds. However, to insure an equilibrium condition, 20 to 30 seconds were allowed before photographing the manometer boards. For each pressure run, a second photograph was taken 5 seconds later. Readings of both photographs consistently agreed within the accuracy of the reading: ± 0.1 cm ($\Delta p = \pm 131 \text{ N/m}^2$ (± 0.019 psi)). The resulting uncertainties in terms of free-stream static pressures vary from $\pm 0.01 p_\infty$ for the highest pressure runs to $\pm 0.19 p_\infty$ for the lowest pressure runs.

The temperature time history of each thermocouple was recorded at the rate of 40 readings/second on magnetic tape by an analog-to-digital data-recording system. These histories were used to obtain the temperature rise rates (dT_w/dt), and these were used to obtain the heating rates (q_w) from

$$q_w = \rho_m c_m \tau_m \frac{dT_w}{dt} \quad (1)$$

where ρ_m and c_m are the density and specific heat of the model material (stainless steel), and τ_m is the thickness of the thin wall (0.076 cm). Second degree polynomials were fitted to the wall temperature readings, taken when the model was positioned in the uniform flow of the test section. During injection the model passes through the shear layer and enters the tunnel uniform-flow core within 0.2 second. The temperature rise rates were taken at the midpoints of the curve fit polynomials.

The error in the heat-transfer data due to longitudinal conduction was checked for the case of the spherical generator 1.27 cm above the plate at a unit Reynolds number of 110×10^6 per meter. The peak heating for this case has the highest level of heat-transfer coefficient of all the data reported and should have the largest conduction error at the

point of peak heating. The analysis of the conduction first considered the heat balance to an element of thin skin which is:

$$\rho c_p dz \frac{\partial T_w}{\partial t} = h(T_{aw} - T_w) - dz \left(k \frac{d^2 T}{dx^2} \right) \quad (2)$$

Heat stored = Aerodynamic heat in + Heat gained by conduction

The conduction term on the right-hand side of equation (2) must be evaluated and compared with the heat stored term. The second derivative in the conduction term was evaluated from the temperature data by a three-point method which would give a maximum value of d^2T/dx^2 at the point of peak heating, and the second derivative was also evaluated from second and fourth order polynomial curve fits of the temperature as a function of x distance and evaluated at the peak heating. A comparison of the three values of d^2T/dx^2 showed that the three-point method and the second order polynomial were approximately the same and gave the largest values. The second derivatives were evaluated at various times and increased with increasing time. The largest value of d^2T/dx^2 was used to evaluate the conduction term at various times. The results of the conduction error check showed that if the heat-transfer data were evaluated at approximately 0.3 second after the start of heating, then the maximum conduction error is 1.7 percent of the indicated heat stored term. For all other peak heating data, the conduction error is less. Therefore, because the conduction error was found to be so small, it was neglected in the reduction of the heat-transfer data.

The experimental heat-transfer coefficient was thus calculated from

$$h = \frac{q_w}{T_{aw} - T_w} \quad (3)$$

where

$$T_{aw} = T_\infty + r(T_t - T_\infty) \quad (4)$$

Because of the prevalence of turbulent boundary layers in these experiments, the turbulent recovery factor was used in calculating the adiabatic wall temperature for the reduction of all the heating data; that is, $r = N_{Pr}^{1/3} \approx 0.90$ (evaluated at the measured wall temperatures).

The heat-transfer data were obtained during the initial heating of the model, while the wall was relatively cool ($T_w \approx 0.6T_t$). However, the long time required for the

pressure readings to stabilize resulted in the pressures being recorded when the model wall was relatively hot ($T_w \approx 0.9T_t$). Thus, the heating distributions were obtained on cool walls, whereas the pressure distributions were obtained on hot walls. Of course, this difference in conditions is undesirable, because wall temperature affects both boundary-layer transition and separation. This effect must be kept in mind when examining and comparing the heating-rate and pressure distributions.

EXPERIMENTAL RESULTS

Interaction Flow Model

A sketch of the interaction of a shock wave incident to a turbulent boundary layer is shown in figure 4, along with typical pressure and heating-rate distributions. In the absence of a boundary layer, the incident shock wave compresses and turns the free-stream flow, strikes, and is reflected from the wall, and further compresses the stream flow. The presence of a boundary layer on the surface complicates the interaction. The incident shock pressure rise causes the boundary layer to separate from the surface upstream of the location (x_s) where the shock would impinge on the surface if there were no boundary layer. As indicated in figure 4, this upstream extent of separated flow is referred to as l_{sep} . The pressure rises at separation to a turbulent plateau value, and then rises to a peak value in the vicinity where the boundary layer reattaches to the surface. The boundary-layer thickness is reduced at reattachment. In the vicinity of reattachment, there are large peak pressures and very large peak heating rates.

Flat-Plate - Free Stream

Undisturbed flow. - Undisturbed (no shock generator) pressure and heating-rate distributions on the flat-plate surface were measured for all five nominal tunnel stagnation pressure levels. These measurements were used as reference conditions to determine the pressure rises and heating amplifications caused by the generated shock-wave-boundary-layer interactions.

The measured heat-transfer distributions, expressed in terms of Stanton number as

$$N_{St,\infty} = \frac{h}{c_p \rho_\infty V_\infty} \quad (5)$$

where c_p is the specific heat, ρ_∞ is the density, and V_∞ is the velocity of the free-stream flow, are plotted in figure 5 for three Reynolds numbers. The distributions are characteristic of transitional-turbulent boundary-layer heating distributions on flat plates, and are compared with the theoretical distribution calculated by using an implicit finite-difference scheme of Anderson and Lewis (ref. 30) which can be used to calculate the

laminar, transitional, and turbulent boundary layers. Boundary-layer transition moves upstream for the higher total pressure levels, as expected, and at the two highest pressure levels the boundary layer is characteristically turbulent over approximately two-thirds of the extent of instrumentation on the flat-plate surface ($22 \text{ cm} < x < 39 \text{ cm}$).

For two of the Reynolds numbers in figure 5, the Anderson-Lewis theory reaches the peak turbulent heating at a point slightly upstream of the data, because the theoretical location of the end of transition did not match the experimental value. The data and the theory both exhibit a peak in heating at the start of fully developed turbulent flow. A composite plot of the heat transfer on the flat plate for the four highest Reynolds numbers is shown in figure 6 in which a peak at the beginning of turbulent heating is indicated for all the data. The magnitude of the peak in heating at the start of fully turbulent flow is evident from the amount the data are above the Spalding-Chi theory (ref. 31); the calculation was made by using a Reynolds number based on distance from the leading edge. The difference between the data and theory at peak heating is believed to be a result of the theory neglecting the fact that the upstream portion of the flow is made up of a laminar and transitional boundary layer. These peaks in heating above flat-plate theory have been observed and discussed by Bertram and Neal (ref. 32), and by Neal (ref. 33), and can be predicted by a simple flat-plate theory if the correct virtual origin for turbulent flow is selected. For a given unit Reynolds number, the data in figure 6 approached the Spalding-Chi theory in the downstream part of the fully turbulent boundary layer.

Shock impingement. - As noted in the previous section, cooling the boundary layer usually delays transition. Thus, transition is believed to have occurred earlier for the pressure experiments ($T_w \approx 0.9T_t$) than for the heat-transfer experiments ($T_w \approx 0.6T_t$). Disturbances, such as the generator shock waves, also cause transition to occur earlier; transition in free shear layers (the separated boundary layer) occurs earlier than for attached boundary layers (ref. 34).

In most cases, it is believed the boundary layer was turbulent at reattachment. However, for the further upstream shock generator locations and lower tunnel pressure levels, the boundary layers were probably transitional in the region of separation. This is particularly true for the heat-transfer data, which were obtained during the initial heating of the model (cold wall).

Schlieren flow photographs showing the entire interaction flow region, including reattachment, could only be obtained for the upstream shock generator locations. (See fig. 7.) The tunnel window fairing obscured the reattachment regions for the downstream generator locations. All of the pressure data and much of the heat-transfer data were obtained with the shock generators in their furthest downstream locations. Thus, these schlieren photographs do not correspond to the interaction data plotted herein. Indeed,

examination of the schlieren photographs in figure 7 reveals that the extent of separated flow decreases with increasing unit Reynolds number for each shock generator. This trend indicates transitional separation (boundary-layer transition occurs between separation and reattachment). (See refs. 17 and 35.) The thrust herein is toward investigating turbulent separation (boundary-layer transition occurring prior to separation); therefore, the downstream shock generator locations were used in most cases. It is unfortunate that schlieren flow photographs of the interaction region could not be obtained for these cases.

Pressure distributions were obtained only for the furthest downstream locations of the shock generators. In these cases, the boundary layer was fully turbulent prior to separation at even the smallest free-stream Reynolds number. The measured pressures for both the disturbed and undisturbed flat-plate flows were first referenced to the free-stream static pressure in order to minimize effects caused by minor variations in p_∞ from run to run, and then the ratios of these pressures were used as the interaction pressure distribution:

$$P \equiv \frac{(p/p_\infty)_{\text{disturbed}}}{(p/p_\infty)_{\text{undisturbed}}} \quad (6)$$

Wedge shock generators.- Interaction pressure distributions for the 10° wedge shock generator are plotted in figure 8. The unit Reynolds numbers shown are those for the tunnel runs with the shock generator installed. (The unit Reynolds numbers for the corresponding undisturbed flow tunnel runs were within 10 percent of those shown for the disturbed flow tunnel runs.) The pressure rises abruptly to a value somewhat larger than that calculated inviscidly. There is a small additional pressure rise further downstream. This rise is attributed to the plate bow wave striking and being reflected by the wedge shock generator, and then impinging on the flat plate. This small additional pressure rise is followed immediately by the drop in pressure caused by the expansion fan from the trailing edge of the shock generator. In figure 8 the inviscid pressure rise and the location of shock impingement on the plate surface are indicated by dashed lines.

The heat-transfer distributions for both the undisturbed flows and for the 10° wedge shock interactions are plotted in figure 9. At the lowest Reynolds number ($R = 17.2 \times 10^6/m$), the undisturbed heating distribution is characteristic of transitional boundary-layer flow. However, the heating distributions for the three highest Reynolds numbers are characteristic of fully turbulent boundary-layer flow over the aft half of the plate. The interaction heating rate initially drops below the undisturbed value for the lowest Reynolds number case, typical of laminar and transitional separation. No similar local regions of decreased heating occur for the three higher Reynolds number cases. As in the pressure distributions, there is a small second rise in the

heating distributions just upstream of where the heating rates start to decrease. This condition is caused by the small additional pressure rise attributed to the reflected plate bow wave.

Distributions of the interaction (disturbed) to undisturbed pressure ratios P , and the interaction and undisturbed heat-transfer rate coefficients for the 12.5° and 15° shock generators are plotted in figures 10 to 13. These distributions follow the same general trends as described above for the 10° shock generator. Of course, the pressure and heating-rate rises are larger for the stronger shock-wave cases. These distributions are for the furthest downstream incident shock location (largest x_s). In every case for the three highest tunnel flow unit Reynolds numbers, the boundary layer was fully turbulent throughout the interaction region. Heating distributions were also obtained for two further upstream locations of the wedge shock generators.

The inviscid, incident shock impingement locations on the flat-plate surface (x_s) are shown in table II(a) for the various wedge shock generators. The unit Reynolds numbers (per meter), total temperature, and wall to total temperature ratios are listed for each heat-transfer tunnel run. The ratio of the peak heating rate to the undisturbed heating rate ($H_{pk} = h_{pk}/h_{undisturbed}$) and the corresponding location x_{pk} of the peak heating rate are also listed. The pressure tunnel runs were made only for the downstream shock generator locations. As evidenced in table II, the unit Reynolds numbers for the pressure runs approximate those for the corresponding heat-transfer tunnel runs. However, the ratios of wall temperature to total temperature for all pressure runs were approximately 0.90. The location and value of the peak interaction pressure ratio are listed. For each of the three highest Reynolds numbers (fully turbulent separation), the extent (l_{sep}) of the pressure rise upstream of the incident shock location (x_s) is indicated. These lengths are referenced to the calculated (ref. 30) undisturbed boundary-layer thicknesses (δ_0) at the start of the interaction region (these thicknesses are approximately half as large as the interval between instrumentation locations on the flat-plate surface). Finally, figure numbers are listed for the data plots shown herein.

Spherical-shock generator. - The interaction pressure ratio distributions for the "higher" spherical-shock generator ($a_s = 2.54$ cm) are plotted in figure 14. In these cases there are very abrupt pressure rises to a single measured peak value (for each Reynolds number), whereupon the pressure then abruptly falls. Of course, the spherical shock wave curves continuously, and the flow passes through a strong expansion fan immediately downstream of the shock. Because of the very abrupt, spikelike pressure distributions, it is unlikely that the true peak pressure occurred precisely at a pressure tap location. Thus, the true peak pressures must be assumed to be somewhat larger than those plotted in figure 14 and shown in table II(b). The inviscid shock impingement

locations x_g were calculated by using an inverse-solution method for sphere-cylinders. (See refs. 36 and 37.)

Plots of the corresponding heating-rate distributions are shown in figure 15. For the two lowest Reynolds numbers the boundary layer is transitional throughout the interaction region. The interaction heating distributions in these cases exhibit the characteristic initial decrease below the undisturbed values at the start of the interaction. There are no local regions of reduced heating for the three highest Reynolds numbers for which the boundary layer was fully turbulent throughout the interaction region.

The strongest shock interaction was generated by the sphere in proximity ($a_g = 1.27$ cm) to the flat plate. The pressure and heating-rate distributions for these interactions (figs. 16 and 17) have the largest gradients and lead to the largest pressure and heating-rate amplifications. A second (much smaller) peak is apparent in both the pressure and heating-rate distributions. These peaks are associated with a reflected shock wave from the sphere-cylinder generator impinging on the flat-plate surface.

Tunnel Wall

In order to obtain interaction data for running length Reynolds numbers comparable to those expected for flight vehicles, experiments were conducted by using an instrumented section of the wind-tunnel wall as the receiver for the wedge and sphere-generated shock waves. In addition to providing thick boundary layers ($4 \text{ cm} < \delta_0 < 6 \text{ cm}$), these interaction data provide the extremely wide range of flow conditions necessary to verify or correct empirical correlations.

Undisturbed flow. - Similar to the flat-plate free-stream experiments, undisturbed pressure and heating-rate distributions on the tunnel wall were measured for five nominal tunnel stagnation pressure levels. These were used as reference conditions for the generated shock interaction pressure and heating-rate amplifications. Schlieren flow photographs of these interactions could not be obtained because the tunnel wall is outside the window field of vision.

The variation of boundary-layer thickness on the tunnel wall with Reynolds number is shown in figure 18. The data points are taken from the tunnel wall boundary-layer surveys of Jones and Feller. (See ref. 29.) The equation faired through these points (see fig. 18) was used to calculate the undisturbed boundary-layer thicknesses used herein. Boundary-layer thicknesses calculated by using the theory of Anderson and Lewis (ref. 30), with edge Mach numbers and pressures from the method of characteristics nozzle design program, were approximately 30 percent less than the measured values. The thinner boundary layers predicted by the Anderson-Lewis program resulted in correspondingly higher predicted heat-transfer rates on the tunnel wall.

Wedge shock generators.- As expected, the thick tunnel wall boundary layers substantially spread out the pressure rises caused by the interaction of the shock wave with the boundary layer. (See fig. 19.) There are "plateaus" in the pressure rises which approach the turbulent plateau pressure rise given, for example, by Sterrett and Emery (ref. 38) as

$$\frac{P_{pl}}{P_1} = 0.091M_1^2 - 0.05 + \frac{6.37}{M_1} \quad (7)$$

This empirical expression is valid only for $M_1 > 3.3$. The value for $M_1 = 6$, $P_{pl}/P_1 = 4.3$, is indicated by the horizontal dashed line in figure 19.

The incident shock location \hat{x}_s is indicated by the vertical dashed line in figure 19. The peak pressures occur close to the location of \hat{x}_s on the tunnel wall. However, these peak pressure ratios are substantially less than that calculated inviscidly. (See figs. 8 and 19.) The thick tunnel wall boundary layers allow the pressure relief associated with the expansion fan from the wedge trailing edge to propagate forward and diminish the peak pressure. The heat-transfer distributions on the tunnel wall, for the undisturbed flows as well as for the 10° wedge shock interaction flows, are plotted in figure 20. Oil film flow observations indicated nearly straight separation and reattachment regions; thus, the transverse curvature effects were negligible.

The interaction pressure ratio distributions and the heat-transfer coefficient distributions for the 12.5° and 15° wedge shock generators (figs. 21 to 24) follow the same general trends as for the 10° wedge shock generator. Of course, the peak interaction pressure ratios, the peak heating amplifications, and the extent of the separated flow increase with increasing generator shock strength.

The experimental results for the wedge-generated shock waves impinging on the tunnel wall are summarized in table III(a). In terms of initial boundary-layer thicknesses, the extent of separation ahead of \hat{x}_s for these tunnel wall tests are comparable to those for the free-stream flat-plate experiments for the same peak pressure rises P_{pk} . (See tables II and III.) For the 15° wedge shock generator, separation occurred upstream of the instrumented section of the wind-tunnel wall; this fact precluded obtaining l_{sep} for these cases.

Spherical shock generator.- Distributions of the interaction pressure ratios and heat-transfer coefficients for the spherical-shock wave generator are plotted in figures 25 to 28. In these cases, the peak pressure ratios, as well as the greatest heating-rate amplifications, occurred just upstream of the (inviscidly) calculated shock-impingement locations. For the strongest generated shock wave ($\hat{a}_s = 2.54$ cm, fig. 28), there are small secondary peaks in the interaction heat-transfer coefficient distributions. These

peaks are associated with compression waves being reflected from the shock generator and interacting with the tunnel wall boundary layer.

The distance between the tunnel wall and sphere is comparable to the thickness of the tunnel wall boundary layer. Therefore, in all these cases, the sphere shock is predominantly within the rotational flow shear layer of the thick tunnel wall boundary layers. This location reduces the shock strength and results in the very small (ℓ_{sep}/δ_o) values shown in table III(b). This condition must be taken into account when comparing the experimental results with analytical ones, and when using the experimental results in extending or modifying empirical correlations.

THEORETICAL ANALYSES, COMPARISONS, AND CORRELATIONS

Free Interaction Pressure Rises

Although the extent of separation and the total-pressure rise depend strongly on the shock strength, the initial pressure rise to the plateau value should be independent of the mechanism generating the shock wave. This concept of a "free interaction" between the viscous boundary layer and the inviscid external flow in the upstream part of the interaction region has been well established for a limited range of Reynolds numbers. (See refs. 17, 18, and 39.)

Initial pressure rises for the 10° and 12.5° wedge shocks impinging on the tunnel wall boundary layers are indicated in figure 29. The pressure ratios are plotted against $(\hat{x} - \hat{x}_o)/\hat{x}_o$, where the subscript o indicates conditions at the upstream location where the disturbance pressure rise begins. The pressure rise curves, thus shifted so that they all start at $\hat{x} = \hat{x}_o$, are all very similar. There is no consistent Reynolds number effect. However, the 10° wedge shock data indicate a somewhat larger pressure gradient than the 12.5° wedge shock data do. Unfortunately, the 15° wedge shock data cannot be included in figure 29 because the pressure rises started upstream of the instrumentation region (see fig. 23), and therefore the values of \hat{x}_o could not be determined for these cases.

The effects of the different wedge shock generator angles are eliminated by plotting the data in terms of the universal similarity function $F(s)$ suggested by Carrière, Sirieix, and Solignac (ref. 18)

$$F(s) = \left[\frac{2(P - 1)}{\gamma M_o^2} \frac{\Delta \nu}{c_{f,o}} \right]^{1/2} \quad (8)$$

where $s \equiv (\hat{x} - \hat{x}_0)/(\hat{x}_f - \hat{x}_0)$, $\Delta\nu$ is the change in the Prandtl-Meyer angle for isentropic compression $\Delta\nu = f(P)$, γ is the ratio of specific heats ($\gamma = 1.4$ herein), $c_{f,0}$ is the coefficient of friction at \hat{x}_0 , and \hat{x}_f is a reference location. This location, which scales the extent of the pressure rise, is determined by requiring that $F = 4.22$ at $\hat{x} = \hat{x}_f$. It has been found (ref. 18) that by using this empirical value, turbulent-boundary-layer pressure rises correlate well for a wide range of test conditions.

In figure 29, the pressure rises are all forced through $P = 1$ at $\hat{x} = \hat{x}_0$; in figure 30, the pressure rises are all forced through $F = 4.22$ at $\hat{x} = \hat{x}_f$. Although the similarity function F does eliminate effects of different wedge shock generator angles, there remains a small and inconsistent Reynolds number effect. Included in figure 30 is the free interaction pressure rise curve suggested by Erdos and Pallone (ref. 39) for turbulent boundary layers. The present data exhibit somewhat steeper initial pressure rises than the curves shown in figure 30, although the data for the intermediate Reynolds numbers ($Re_{\hat{x}} = 211 \times 10^6$ and 213×10^6) fall close to the curves for both wedge angles.

Elfstrom (ref. 10) and Reeves (ref. 19) observed increases in turbulent plateau pressures with increasing separation lengths. This condition holds true for separation lengths up to 10 times as long as the undisturbed boundary-layer thickness. The data herein support this trend. (See figs. 19, 21, and 23.) However, as noted by Reeves (ref. 19) and also by Whitehead, et al. (ref. 4), three-dimensional flow effects are important and can alter the trends established for two-dimensional flows.

Separation Lengths

The separation lengths listed in tables II and III, nondimensionalized with respect to the undisturbed boundary-layer thicknesses at the start of the interaction regions, are plotted against peak pressure rise ratios in figure 31. These results can be approximated very simply by

$$\frac{l_{sep}}{\delta_0} = \frac{P_{pk}}{3} \quad (9)$$

for $M_1 = 6$ and Reynolds numbers from 10^7 to 4×10^8 . The open circle symbols in figure 31 are for the sphere-generated shock waves impinging on the thick tunnel wall boundary layer. In these cases most of the sphere shock is within the rotational flow of the boundary layer; this fact makes questionable the use of $M_1 = 6$ as the effective free-stream Mach number. With the exception of these points, the remaining data (for these particular test conditions) follow equation (9). The data scatter for the sphere-generated shock waves impinging on the flat-plate boundary layer can result from the true peak pressure not being measured (see figs. 14 and 16) or from lateral relief of the separation region.

Williams (ref. 13) and Mikesell (ref. 14) established expressions for turbulent separation lengths in terms of the peak pressure p_{pk} and the turbulent plateau pressure and corresponding Mach number p_{pl} and M_{pl} . Williams presented his separation length data as a function of the parameter

$$f_1(p_{pk}, p_{pl}) \equiv \frac{p_{pk} - p_{pl}}{p_{pl} M_{pl}^2} \quad (10)$$

whereas Mikesell presented his data as a function of the parameter

$$f_2(p_{pk}, p_{pl}) \equiv \frac{\left[1 + \frac{\gamma - 1}{2} M_{pl}^2 - \left(\frac{p_{pk}}{p_{pl}} \right)^{\frac{\gamma - 1}{\gamma}} \right]}{\frac{\gamma - 1}{2} M_{pl}^2 \left(\frac{p_{pk}}{p_{pl}} \right)^{\frac{\gamma - 1}{\gamma}}} \quad (11)$$

The separation lengths are functions of these parameters. These functions are shown in figure 32 along with the experimental results. Because the plateau conditions must be known, only the data for the wedge-generated shock wave impinging on the tunnel wall could be shown in this figure. Also, the 15° wedge data had to be excluded because the extent of separation is not known for these cases. (See fig. 23.)

Peak Heating - Pressure Correlations

The turbulent interference heating correlation shown in figure 33 presents the peak heating ratio as a function of the peak pressure ratio. The peak heating ratio H_{pk} is defined as the peak heating rate for the interaction flow divided by the heating rate for undisturbed flow at the same location. The peak pressure ratio P_{pk} is defined as p_{pk}/p_{∞} for the disturbed flow divided by p/p_{∞} for the undisturbed flow at the same location. The data from the present investigation are shown as various symbols that indicate the nominal unit Reynolds number, type of generator, and whether the test is on the plate or on the tunnel wall. The curved-line shaded area represents data from various investigators presented by Holden in reference 40. The data appear to correlate according to the power law

$$H_{pk} = (P_{pk})^n \quad (12)$$

The same power law correlation has been presented in many previous investigations. The values of n for the best correlations were found to be $n = 0.85$ by Holden (ref. 40) and Markarian (ref. 26); $n = 0.80$ by Sayano (ref. 27), Haslett et al. (ref. 22), and Hung

and Barnett (ref. 21); and $n = 0.71$ by Popinski (ref. 15). The data from the present experiments, which include results for running length Reynolds numbers exceeding 400×10^6 , coupled with the previously reported data shown in figure 33, indicate that the best correlation is achieved by using $n = 0.85$. There are no discernible Reynolds number effects on the correlation for running length Reynolds numbers varying from 2×10^6 to 400×10^6 .

Another correlation, suggested by Bushnell and Weinstein (ref. 25), is shown in figure 34 as

$$\frac{h_{pk}}{\rho_w V_e c_p} \propto \left(\frac{\rho_w V_e \delta_s}{\mu_w \sin \phi} \right)^{-0.2} \quad (13)$$

where $\rho_w V_e$ and μ_w pertain to the reattached flow, δ_s is the thickness of the free-shear layer, ϕ is the turning angle of the flow at reattachment, and subscript e refers to conditions at the outer edge of the boundary layer. The data presented by Bushnell and Weinstein were measured at the reattachment of separated flows on trailing-edge flaps. Their data exhibit lower heating rates than those obtained from the present experiments for reattachment of flows separated by incident shock waves. Included in figure 34 is a correlation of incident shock wave interaction data presented by Keyes and Hains. (See ref. 34.)

CONCLUDING REMARKS

Measurements of pressure and heat transfer in the area of a shock-wave-boundary-layer interaction were obtained on a flat plate in a free stream and on the test-section tunnel wall for Mach 6 and for running-length Reynolds numbers from 2×10^6 to 400×10^6 . The test results were obtained for relatively thin (flat plate) as well as relatively thick (tunnel wall) boundary layers; the thick boundary layers occur at Reynolds numbers comparable with those expected for flight vehicles (running-length Reynolds numbers exceeding 400×10^6).

The highest interference heating for a turbulent boundary-layer interaction was obtained on the flat plate in the presence of a strong shock generated by a sphere-cylinder in proximity to the plate. This interaction resulted in amplification factors, compared with undisturbed values, of 22.1 and 30.3 for heating rates and pressures, respectively. The highest interference heating on the tunnel wall occurred when a shock from a 15° wedge generator impinged on a turbulent boundary layer and resulted in disturbed to undisturbed amplification factors of 11.6 and 15.4 for heating rates and pressures, respectively. For turbulent boundary-layer flow, the peak heating amplification can be estimated from $H_{pk} = (P_{pk})^{0.85}$ where H_{pk} is the peak ratio of the heat-transfer

coefficients and P_{pk} is the peak pressure ratio. There are no discernible Reynolds number effects for Reynolds numbers from 2×10^6 to 400×10^6 .

The initial pressure rises on the tunnel wall follow the turbulent free interaction pressure rise distribution. Free interaction similarity methods adequately account for the effect of different shock strengths. However, the data still showed inconsistent Reynolds number effects.

Separation lengths for these turbulent boundary layers varied approximately linearly with the peak pressure rises. The measured separation lengths are comparable with values calculated using previously established empirical expressions, which are functions of the turbulent plateau pressure and peak pressure.

Langley Research Center,
National Aeronautics and Space Administration,
Hampton, Va., June 3, 1974.

REFERENCES

1. Korkegi, Robert H.: Survey of Viscous Interactions Associated With High Mach Number Flight. *AIAA J.*, vol. 9, no. 5, May 1971, pp. 771-784.
2. Ryan, B. M.: Summary of the Aerothermodynamic Interference Literature. Tech. Note 4061-160, Naval Weapons Center (China Lake, Calif.), Apr. 1969.
3. Gerhart, Philip M.: Heat Transfer Downstream of Attachment of a Turbulent Supersonic Shear Layer. *AIAA J.*, vol. 11, no. 1, Jan 1973, pp. 104-106.
4. Whitehead, A. H., Jr.; Sterrett, James R.; and Emery, James C.: Effects of Transverse Outflow From a Hypersonic Separated Region. *AIAA J.*, vol. 10, no. 4, Apr. 1972, pp. 553-555.
5. Goldberg, Theodore J.: Three-Dimensional Separation for Interaction of Shock Waves With Turbulent Boundary Layers. *AIAA J.*, vol. 11, no. 11, Nov. 1973, pp. 1573-1575.
6. Law, C. Herbert: Supersonic, Turbulent Boundary Layer Separation Measurements at Reynolds Numbers of 10^7 to 10^8 . *AIAA Paper No. 73-665*, July 1973.
7. Rose, William C.; Page, Richard J.; and Childs, Morris E.: Incipient Separation Pressure Rise for a Mach 3.8 Turbulent Boundary Layer. *AIAA J.*, vol. 11, no. 5, May 1973, pp. 761-763.
8. Stollery, J. L.: Laminar and Turbulent Boundary-Layer Studies at Hypersonic Speeds. *ICAS Paper No. 72-09*, Sept. 1972.
9. Spaid, Frank W.; and Frishett, John C.: Incipient Separation of a Supersonic, Turbulent Boundary Layer, Including Effects of Heat Transfer. *AIAA J.*, vol. 10, no. 7, July 1972, pp. 915-922.
10. Elfstrom, G. M.: Turbulent Hypersonic Flow at a Wedge-Compression Corner. *J. Fluid Mech.*, vol. 53, pt. 1, 1972, pp. 113-127.
11. Todisco, A.; and Reeves, B. L.: Turbulent Boundary Layer Separation and Reattachment at Supersonic and Hypersonic Speeds. *Proceedings of the 1969 Symposium on Viscous Interaction Phenomena in Supersonic and Hypersonic Flow*, Univ. of Dayton Press, 1970, pp. 139-179.
12. Roshko, A.; and Thomke, G. J.: Supersonic, Turbulent Boundary-Layer Interaction With a Compression Corner at Very High Reynolds Number. *Proceedings of the 1969 Symposium on Viscous Interaction Phenomena in Supersonic and Hypersonic Flow*, Univ. of Dayton Press, 1970, pp. 109-138.

13. Williams, J. C., III: On the Upstream Length of Turbulent Boundary-Layer Separation. AIAA J., vol. 3, no. 12, Dec. 1965, pp. 2347-2348.
14. Mikesell, R. D.: Length Scale of Separated Turbulent Boundary Layers in Compression Corners. AIAA J., vol. 4, no. 8, Aug. 1966, pp. 1482-1483.
15. Popinski, Z.: Shock Wave-Boundary Layer Interaction. Proceedings of the Third International Heat Transfer Conference - Vol. II, Amer. Inst. Chem. Eng., Aug. 1966, pp. 262-273.
16. Giles, H. L.; and Thomas, J. W.: Analysis of Hypersonic Pressure and Heat Transfer Tests on a Flat Plate With a Flap and a Delta Wing With Body, Elevons, Fins, and Rudders. NASA CR-536, 1966.
17. Chapman, Dean R.; Kuehn, Donald M.; and Larson, Howard K.: Investigation of Separated Flows in Supersonic and Subsonic Streams With Emphasis on the Effect of Transition. NACA Rep. 1356, 1958.
18. Carrière, P.; Sirieix, M.; and Solignac, J.-L.: Similarity Properties of the Laminar or Turbulent Separation Phenomena in a Non-Uniform Supersonic Flow. Applied Mechanics, M. Hetényi and W. G. Vincenti, eds., Springer-Verlag, 1969, pp. 145-157.
19. Reeves, Barry L.: Plateau Pressure in Hypersonic Turbulent Boundary-Layer Interactions. AIAA J., vol. 10, no. 11, Nov. 1972, pp. 1546-1548.
20. Hung, F. T.: Interference Heating Due to Shock Wave Impingement on Laminar Boundary Layers. AIAA Paper No. 73-678, July 1973.
21. Hung, F. T.; and Barnett, D. O.: Shockwave-Boundary Layer Interference Heating Analysis. AIAA Paper No. 73-237, Jan. 1973.
22. Haslett, Robert A.; Kaufman, Louis G., II; Romanowski, Richard F.; and Urkowitz, Michael: Interference Heating Due to Shock Impingement. AFFDL-TR-72-36, U.S. Air Force, July 1972.
23. Neumann, Richard D.: Recent Notes and Data on Interference Heating. AFFDL-TR-72-12, U.S. Air Force, May 1972.
24. Neumann, Richard D.; and Burke, Gerald L.: The Influence of Shock Wave-Boundary Layer Effects on the Design of Hypersonic Aircraft. AFFDL-TR-68-152, U.S. Air Force, Mar. 1969. (Available from DDC as AD 686 738.)
25. Bushnell, Dennis M.; and Weinstein, Leonard M.: Correlation of Peak Heating for Rattachment of Separated Flows. J. Spacecraft & Rockets, vol. 5, no. 9, Sept. 1968, pp. 1111-1112.

26. Markarian, C. Franklyn: Heat Transfer in Shock Wave-Boundary Layer Interaction Regions. NWC TP 4485, U.S. Navy, Nov. 1968. (Available from DDC as AD 849 532.)
27. Sayano, S.: Heat Transfer in Shock Wave-Turbulent Boundary Layer Interaction Regions. Rep. SM-42567, Missile & Space Systems Div., Douglas Aircraft Co., Inc., Nov. 19, 1962.
28. Reda, Daniel C.; and Murphy, John D.: Shock Wave/Turbulent Boundary-Layer Interactions in Rectangular Channels. AIAA J., vol. 11, no. 2, Feb. 1973, pp. 139-140.
29. Jones, Robert A.; and Feller, William V.: Preliminary Surveys of the Wall Boundary Layer in a Mach 6 Axisymmetric Tunnel. NASA TN D-5620, 1970.
30. Anderson, E. C.; and Lewis, C. H.: Laminar or Turbulent Boundary-Layer Flows of Perfect Gases or Reacting Gas Mixtures in Chemical Equilibrium. NASA CR-1893, 1971.
31. Spalding, D. B.; and Chi, S. W.: The Drag of a Compressible Turbulent Boundary Layer on a Smooth Flat Plate With and Without Heat Transfer. J. Fluid Mech., vol. 18, pt. 1, Jan. 1964, pp. 117-143.
32. Bertram, Mitchel H.; and Neal, Luther, Jr.: Recent Experiments in Hypersonic Turbulent Boundary Layers. Presented at the AGARD Specialists Meeting on Recent Developments in Boundary-Layer Research (Naples, Italy), May 1965. (Also available as NASA TM X-56335.)
33. Neal, Luther, Jr.: A Study of the Pressure Heat Transfer, and Skin Friction on Sharp and Blunt Flat Plates at Mach 6.8. NASA TN D-3312, 1966.
34. Keyes, J. Wayne; and Hains, Frank D.: Analytical and Experimental Studies of Shock Interference Heating in Hypersonic Flows. NASA TN D-7139, 1973.
35. Johnson, Charles B.: Pressure and Flow-Field Study at Mach Number 8 of Flow Separation on a Flat Plate With Deflected Trailing-Edge Flap. NASA TN D-4308, 1968.
36. Lomax, Harvard; and Inouye, Mamoru: Numerical Analysis of Flow Properties About Blunt Bodies Moving at Supersonic Speeds in an Equilibrium Gas. NASA TR R-204, 1964.
37. Inouye, Mamoru; Rakich, John V.; and Lomax, Harvard: A Description of Numerical Methods and Computer Programs for Two-Dimensional and Axisymmetric Supersonic Flow Over Blunt-Nosed and Flared Bodies. NASA TN D-2970, 1965.

38. Sterrett, James R.; and Emery, James C.: Extension of Boundary-Layer Separation Criteria to a Mach Number of 6.5 by Utilizing Flat Plates With Forward-Facing Steps. NASA TN D-618, 1960.
39. Erdos, John; and Pallone, Adrian: Shock-Boundary Layer Interaction and Flow Separation. Proceedings of the 1962 Heat Transfer and Fluid Mechanics Institute, F. Edward Ehlers, James J. Kauzlarich, Charles A. Sleicher, Jr., and Robert E. Street, eds., Stanford Univ. Press, c.1962, pp. 239-254.
40. Holden, M. S.: Shock Wave-Turbulent Boundary Layer Interaction in Hypersonic Flow. AIAA Paper No. 72-74, Jan. 1972.

38. Sterrett, James R.; and Emery, James C.: Extension of Boundary-Layer Separation Criteria to a Mach Number of 6.5 by Utilizing Flat Plates With Forward-Facing Steps. NASA TN D-618, 1960.
39. Erdos, John; and Pallone, Adrian: Shock-Boundary Layer Interaction and Flow Separation. Proceedings of the 1962 Heat Transfer and Fluid Mechanics Institute, F. Edward Ehlers, James J. Kauzlarich, Charles A. Sleicher, Jr., and Robert E. Street, eds., Stanford Univ. Press, c.1962, pp. 239-254.
40. Holden, M. S.: Shock Wave-Turbulent Boundary Layer Interaction in Hypersonic Flow. AIAA Paper No. 72-74, Jan. 1972.

TABLE I. - NOMINAL TEST CONDITIONS

P_t		T_t, K	R/m
N/m^2	psia		
0.97×10^6	140	490	8.1×10^6
2.2	315	520	17
4.9	715	530	37
9.8	1415	540	69
18	2615	560	120

TABLE II. - FREE-STREAM FLAT-PLATE EXPERIMENTAL RESULTS - Concluded

(b) Spherical shock generator

Sphere generator			Heat transfer					Pressure				
a_s , m	x_s , m	R/m	T_t , K	T_w/T_t	H_{pk}	x_{pk} , m	Figure	R/m	P_{pk}	x_{pk} , m	$\frac{t_{sep}}{\delta_0}$	Figure
0.0254	0.1549*	8.8×10^6	490	0.62	51.21	0.1547						
	.1552*	18.8	515	.58	72.83							
	↓	37.5	538	.57	63.60	↓						
		74.1	532	.57	27.34	↓						
	.2189	8.6	498	.60	46.29	.2207						
	.2192	18.4	518	.53	46.19	↓						
	↓	33.3	571	.53	17.25	↓						
		75.2	528	.58	15.26	↓						
	.2824	8.8	481	.62	47.58	.2817	15	7.9×10^6	21.8	0.287		14
	.2927	18.2	512	.59	36.73	↓	↓	17.2	24.5	↓		↓
	↓	35.6	544	.55	13.55	↓		34.5	24.0	↓	6	
		74.7	532	.57	15.86	↓		67.7	21.7	↓	7	
	↓	123.4	556	.58	13.89	↓	↓	121.4	22.5	↓	7	↓
	.0127											
.0127	.1493*	9.3	476	.63	73.01	.1445						
	.1496*	18.7	512	.58	96.61	.1445						
	↓	37.1	542	.55	92.48	.1493						
		77.4	521	.57	43.59	.1496						
	.2131	8.8	493	.60	59.25	.2126						
	.2134	18.5	521	.58	60.20	.2156						
	↓	37.4	534	.56	23.43	↓						
		77.2	521	.56	21.96	↓						
	.2771	8.5	490	.62	63.55	.2766	17	7.5	31.5	.277		16
	.2774	17.0	525	.58	41.66	↓	↓	16.4	33.0	.262		↓
	↓	35.2	547	.55	20.48	↓		38.8	32.8	↓	9	
		74.2	532	.56	22.13	↓		65.8	30.3	↓	10	
	↓	110.2	571	.57	19.17	↓	↓	112.2	28.9	↓	11	↓

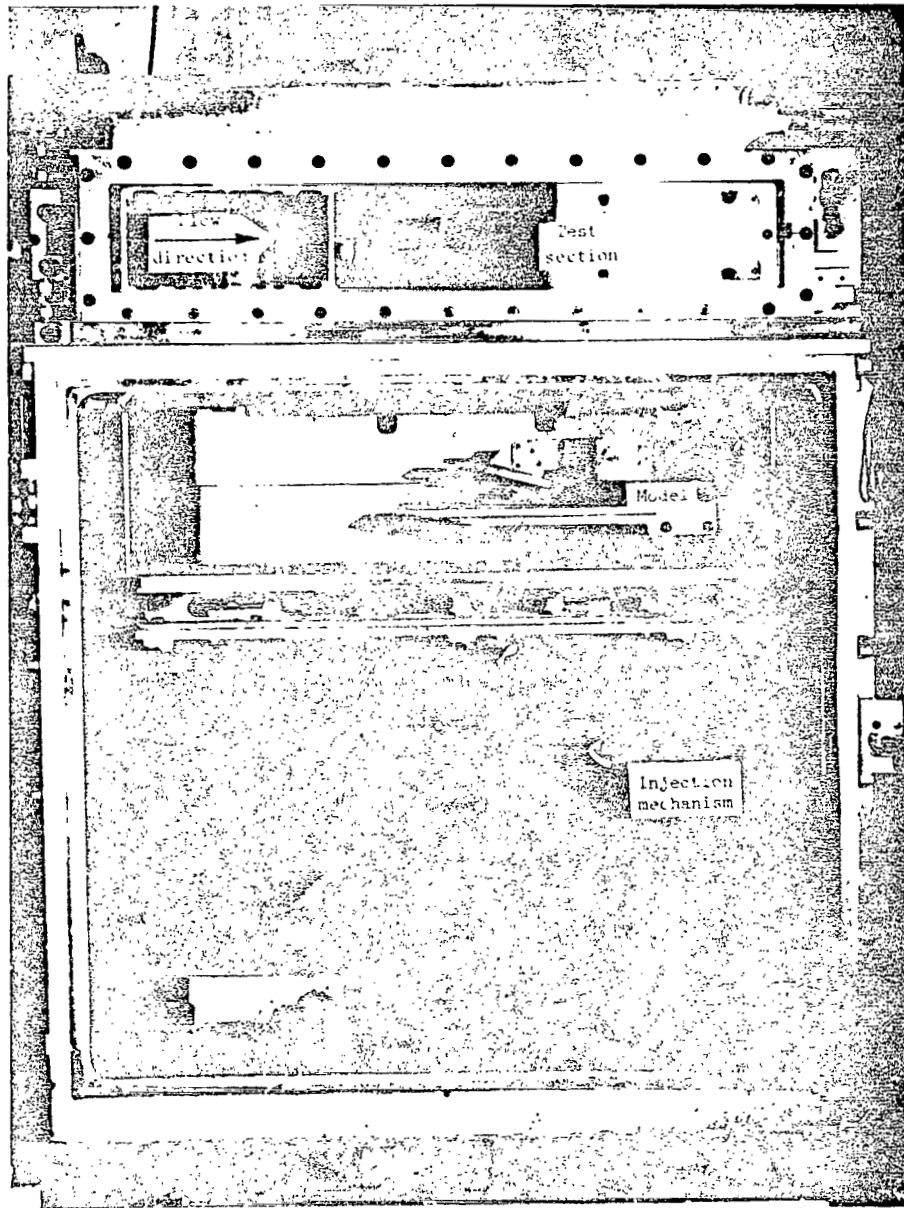
*At the lowest tunnel stagnation pressure level, the tunnel flow Mach number approximately equals 5.9, and results in a slightly different inviscid shock shape than for all other tunnel stagnation pressure levels, for which $M_1 = 6.0$.

TABLE III - TUNNEL WALL EXPERIMENTAL RESULTS - Concluded

(b) Spherical shock generator

Sphere generator		Heat transfer						Pressure				
a_s , m	\hat{a}_s , m	R/m	T_t , K	T_w/T_t	H_{pk}	\hat{x}_{pk} , m	Figure	R/m	P_{pk}	\hat{x}_{pk} , m	$\frac{l_{sep}}{\delta_0}$	Figure
0.0508	3.160*	6.9×10^6	477	0.63	5.09	3.129	26					
↓	3.159	17.5	519	.58	5.24	3.134	↓	18.0×10^6	5.5	3.144	1.0	25
	↓	39.5	543	.56	5.18	3.139		36.9	6.5	3.149	1.0	↓
	↓	78.0	539	.57	4.58	3.139		68.0	7.6	3.142	1.1	
	↓	128.1	554	.58	5.32	3.149	↓	113.4	7.0	3.154	1.0	↓
.0254	3.084*	8.6	490	.61	10.21	3.068						
↓	3.088	18.0	516	.58	9.86	↓						
	↓	40.9	528	.57	9.27							
	↓	40.1	534	↓	8.87	↓						
	↓	78.1	535	↓	7.29	↓						
	3.148*	6.8	495	.61	9.82	3.134	28					
	3.147	18.2	493	.60	9.09	↓	↓	16.5	8.2	3.139	1.0	27
	↓	43.5	506	.59	8.35	↓		35.3	10.1	3.139	1.2	↓
	↓	83.6	513	.59	7.58	↓		64.4	11.6	↓	1.3	
	↓	129.3	556	.58	9.65	3.139	↓	114.6	11.0	↓	1.4	↓

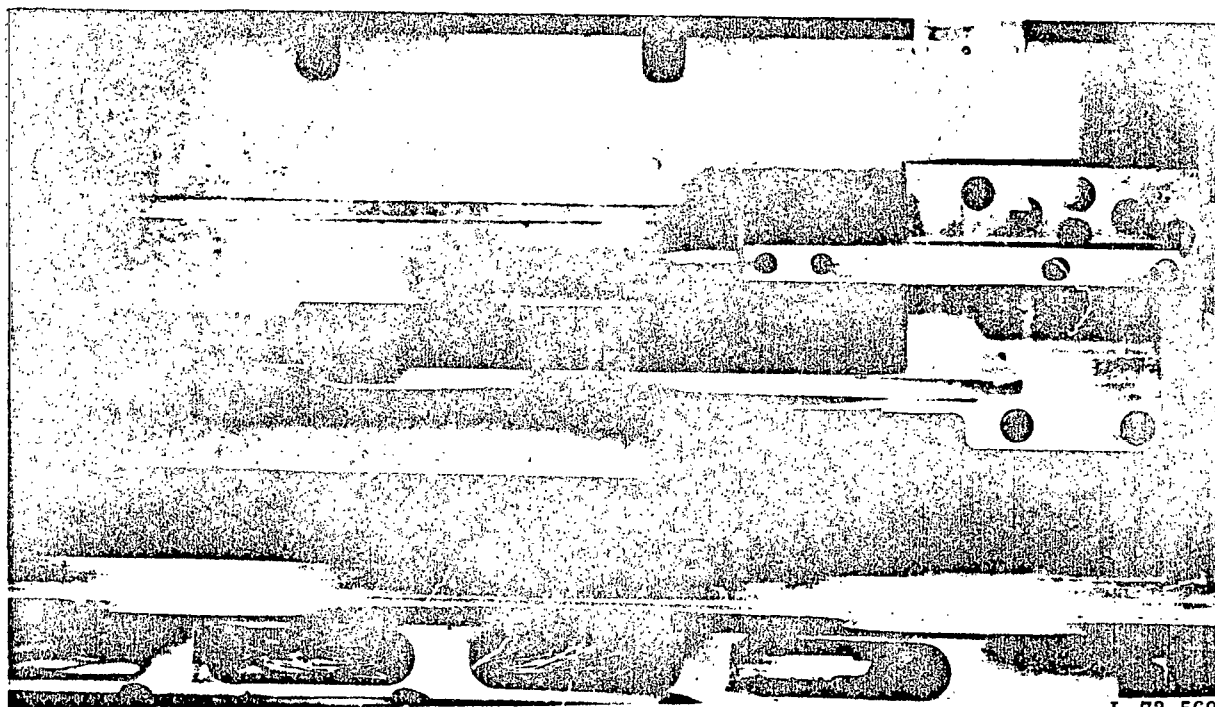
*At the lowest tunnel stagnation pressure level, the tunnel flow Mach number approximately equals 5.9, and results in a slightly different inviscid shock shape than for all other tunnel stagnation pressure levels, for which $M_1 = 6.0$.



L-73-5692

(a) Test section, vacuum tight chamber, and injection mechanism.

Figure 1.- Photographs of Mach 6 tunnel apparatus and model.



L-73-5693

(b) Flat-plate heat-transfer model with sphere generator.

Figure 1.- Concluded.

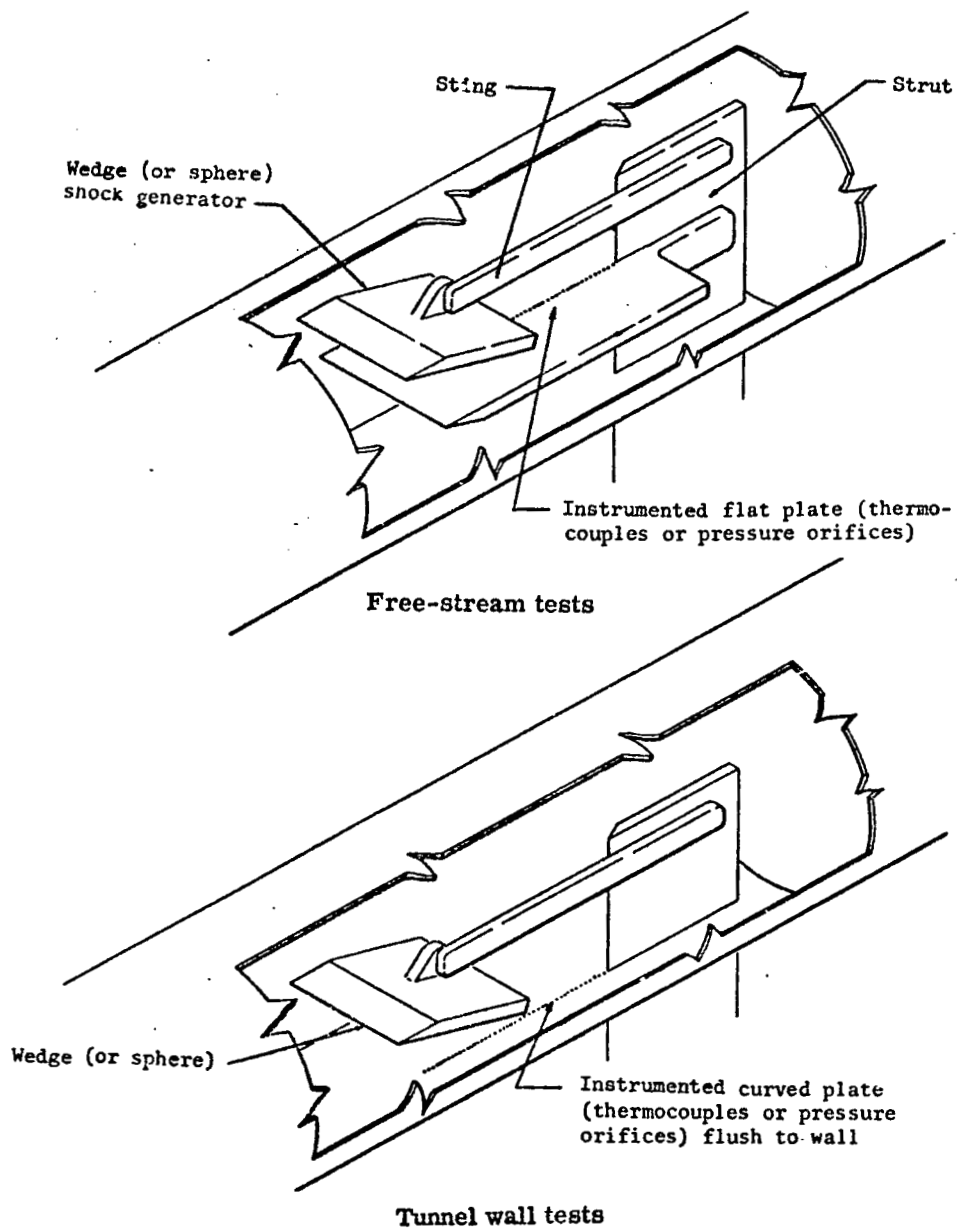


Figure 2.- Model sketches and coordinate system.

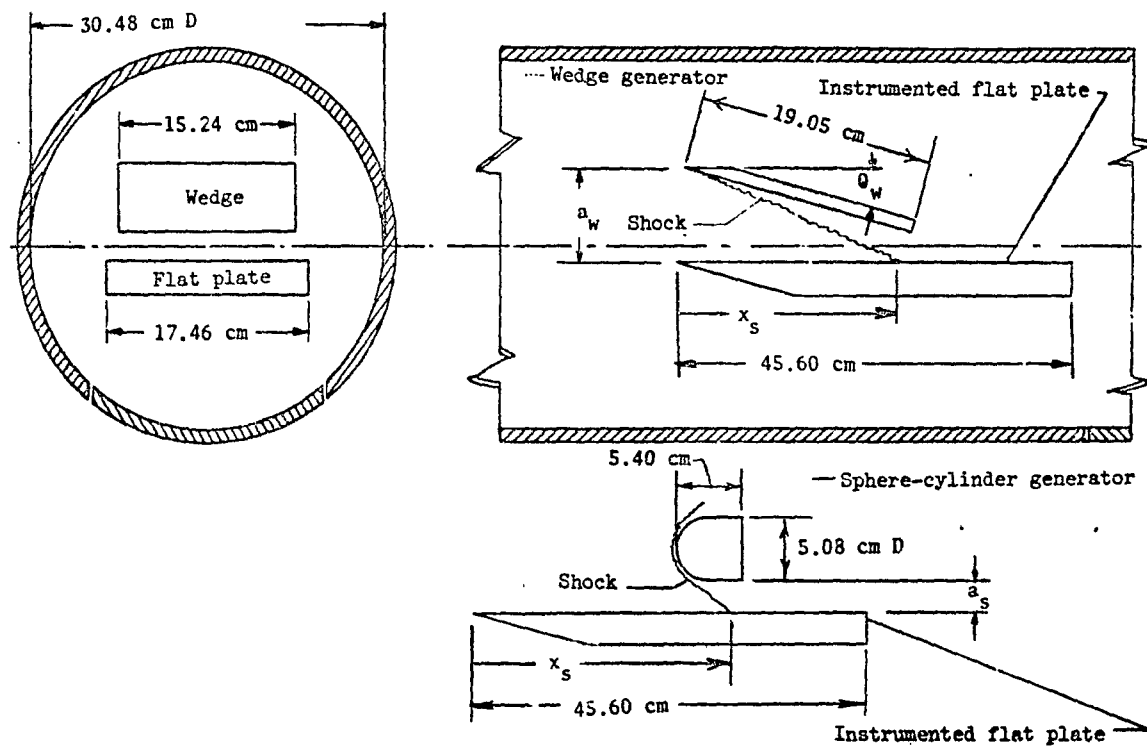


Figure 2.- Continued.

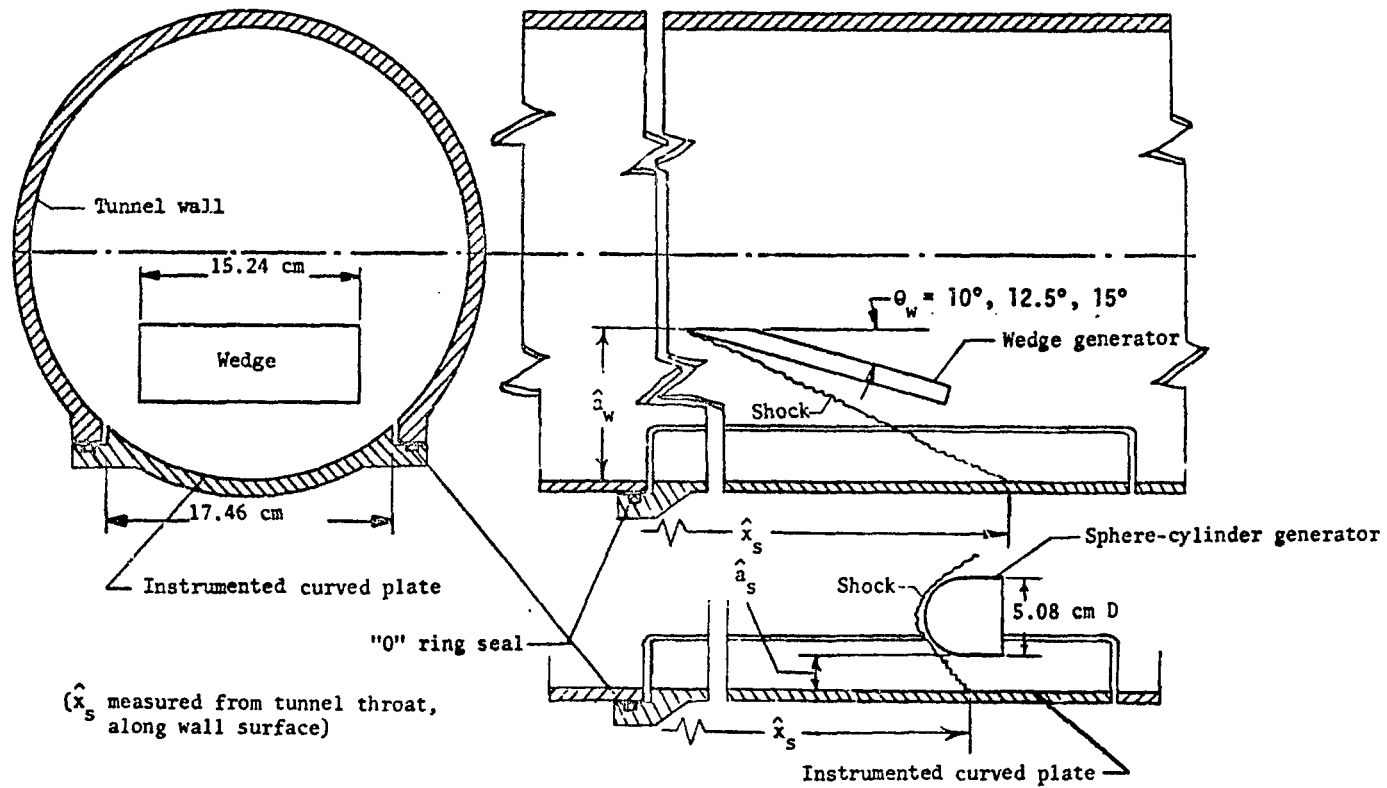
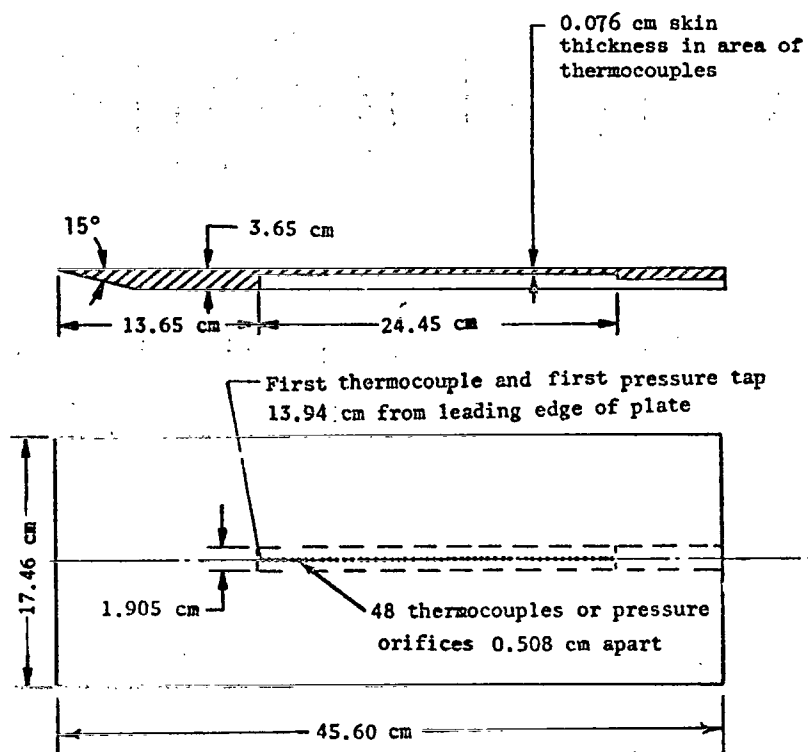
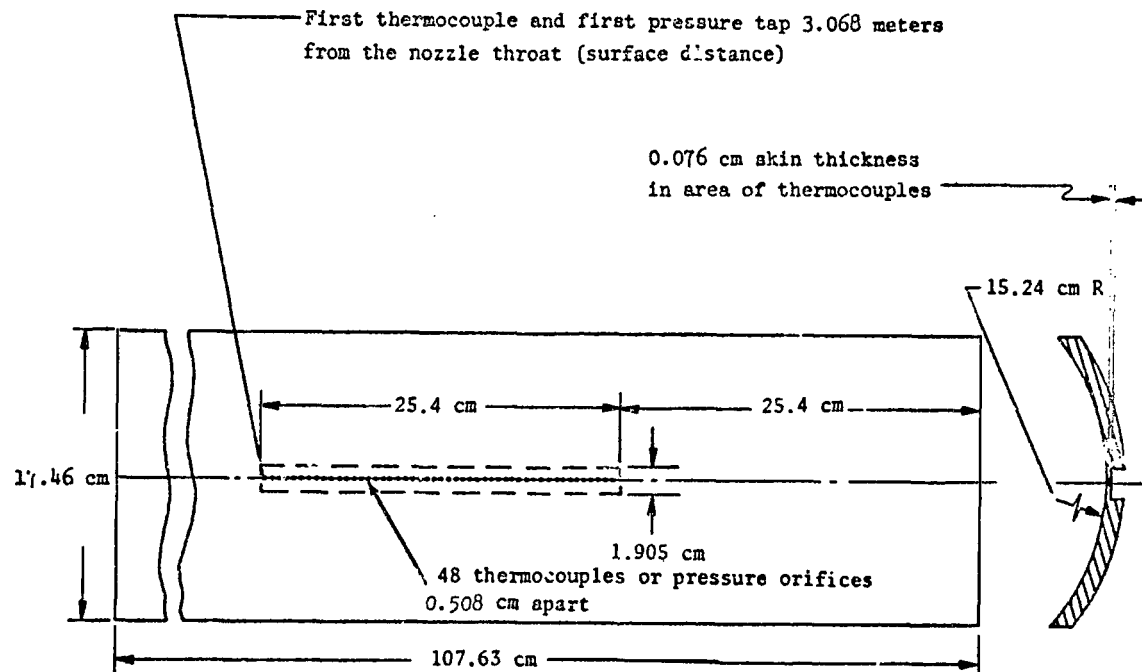


Figure 2.- Concluded.



(a) Flat plate.

Figure 3.- Model instrumentation locations.



(b) Tunnel wall.

Figure 3.- Concluded.

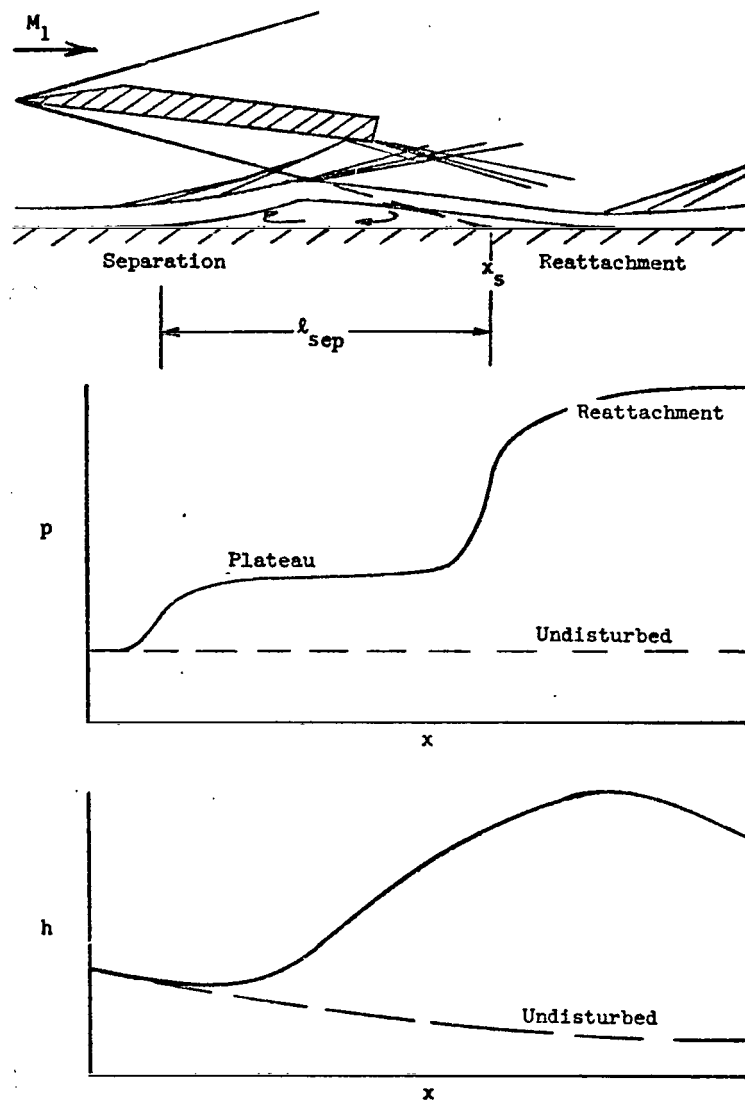


Figure 4.- Sketch of interaction flow and resulting pressure and heating-rate distributions on flat plate or tunnel wall surface.

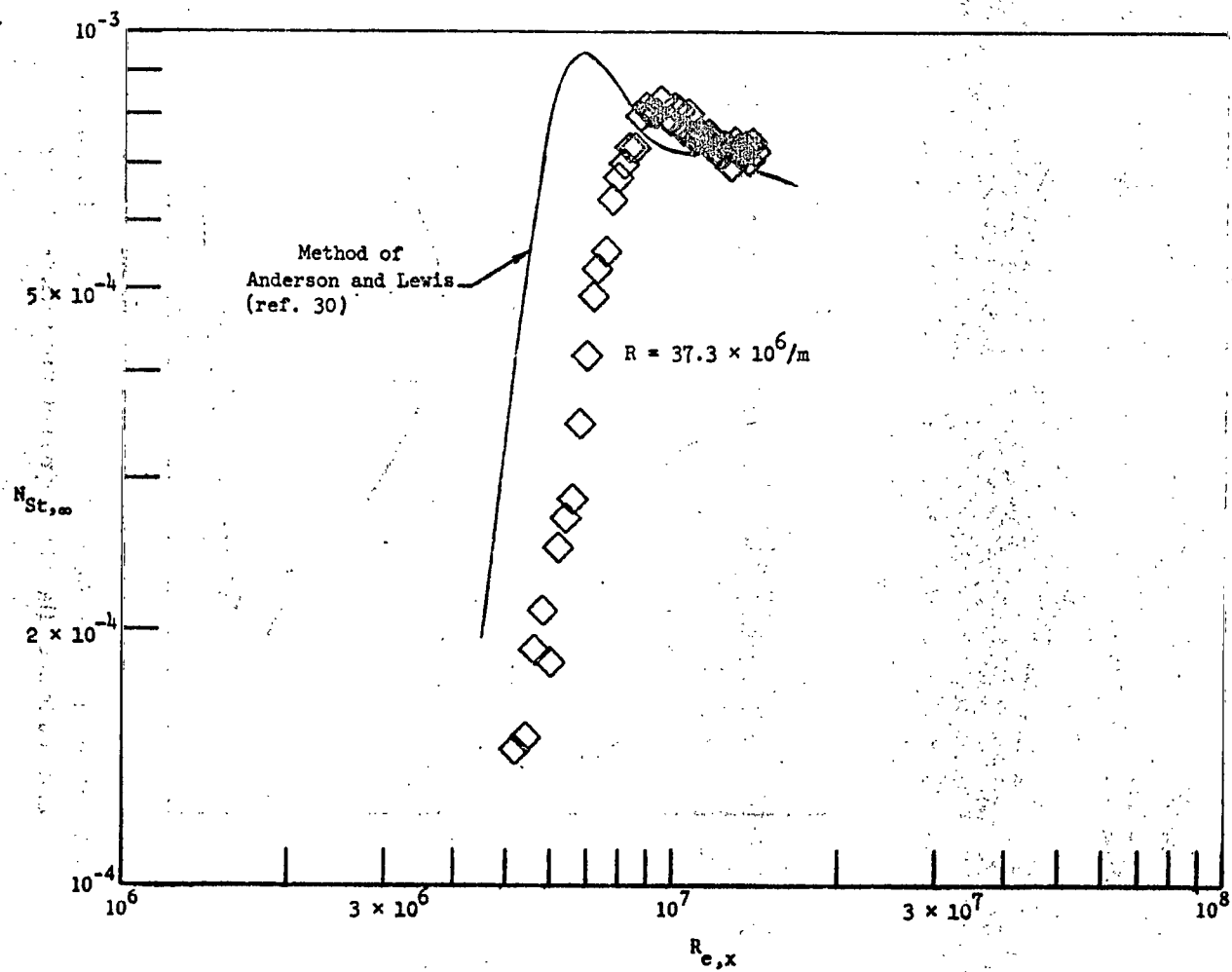


Figure 5.- Transitional and turbulent heating distributions on a flat plate for Mach 6.

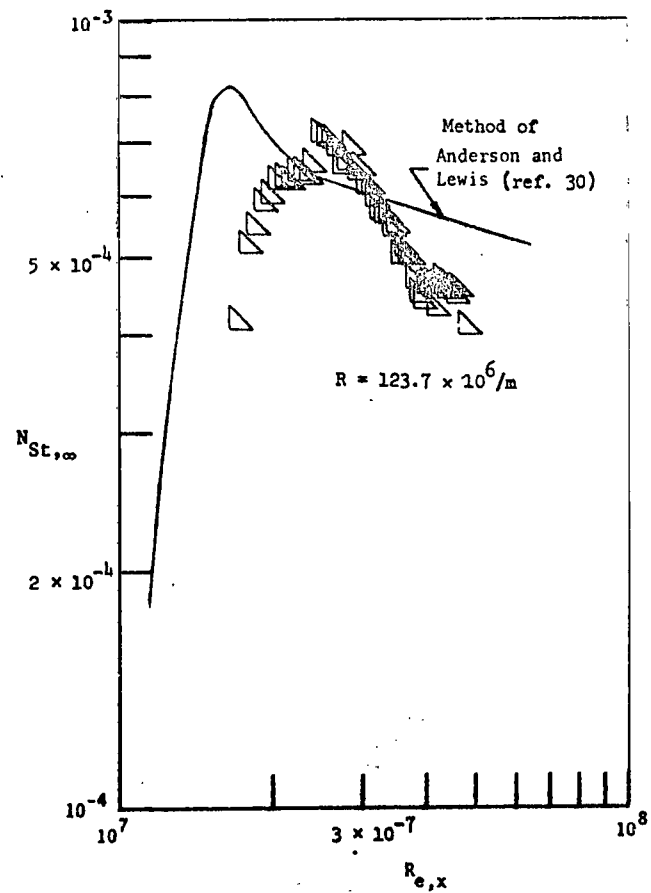
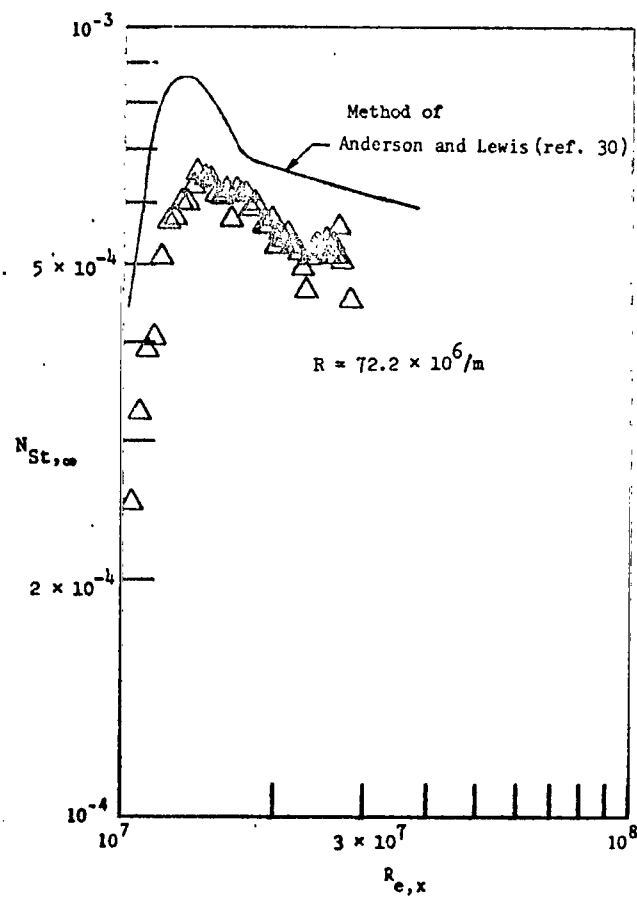


Figure 5.- Concluded.

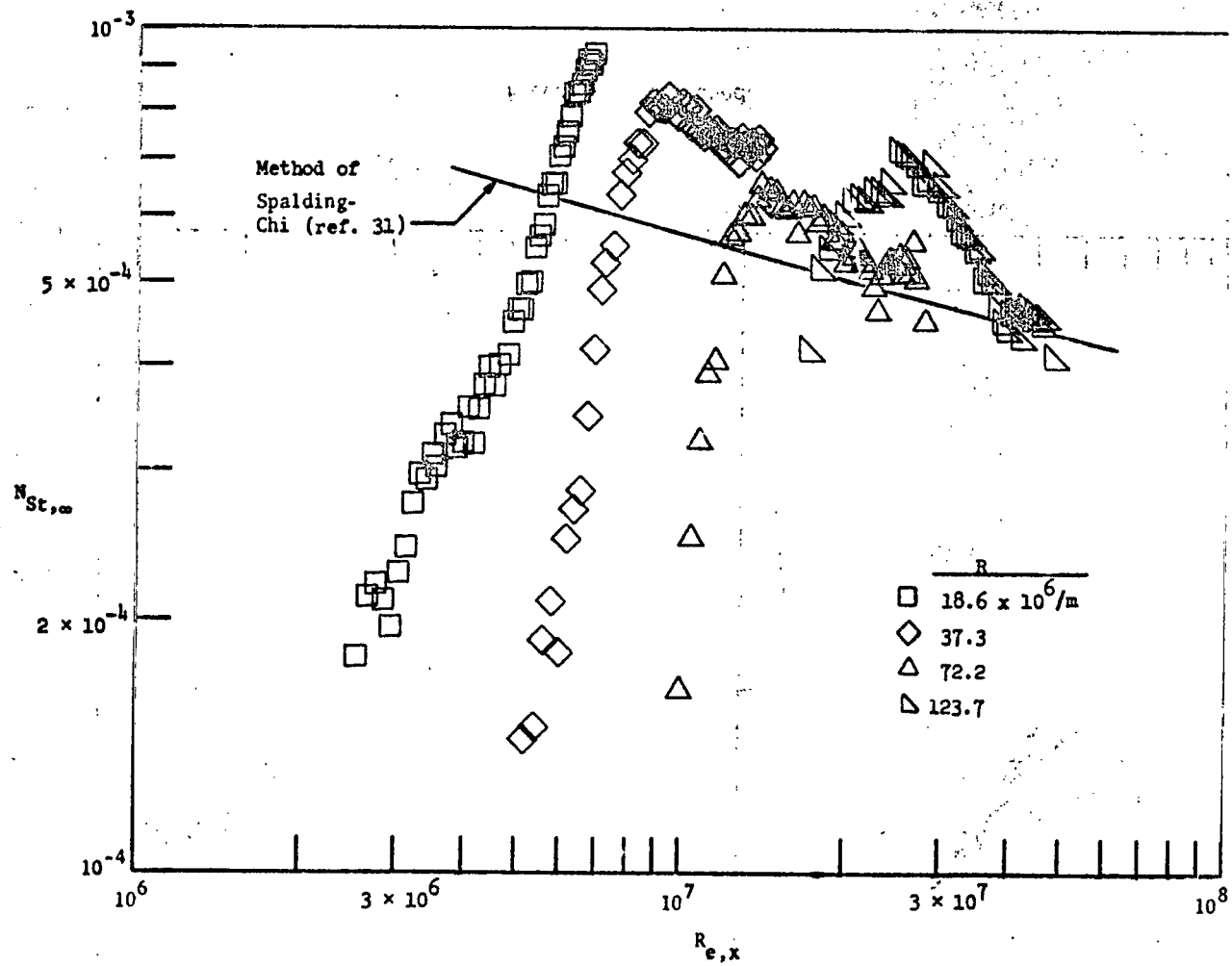
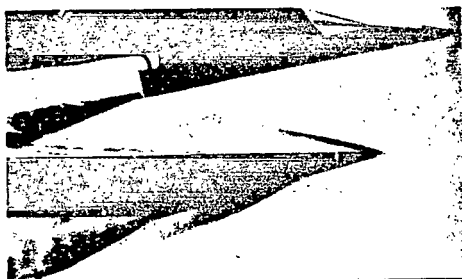
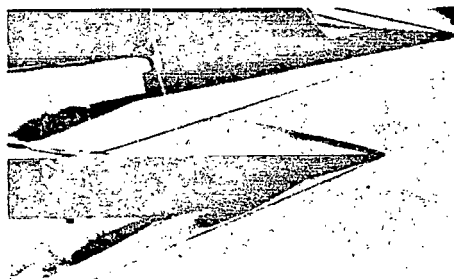


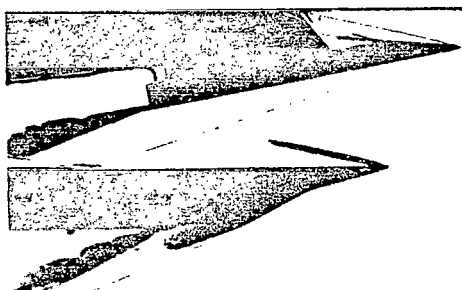
Figure 6.- Transitional and turbulent heating distributions for various unit Reynolds numbers.



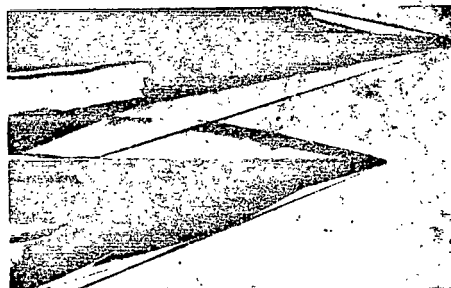
$$R_{x,s} = 19.5 \times 10^6 / m$$



$$R_{x,s} = 37.0 \times 10^6 / m$$



$$R_{x,s} = 73.7 \times 10^6 / m$$



$$R_{x,s} = 140 \times 10^6 / m$$

L-74-1113

(a) 10° wedge generator.

Figure 7.- Schlieren flow photographs, generators in forward position.



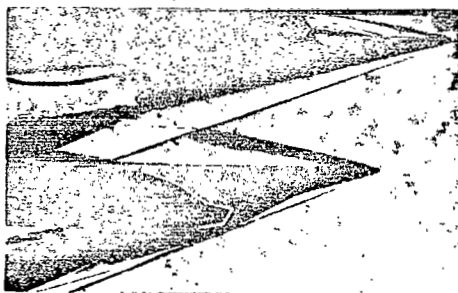
$$R = 19.0 \times 10^6 / \text{m}$$

$$R_{x,s} = 3.28 \times 10^6$$



$$R = 77.0 \times 10^6 / \text{m}$$

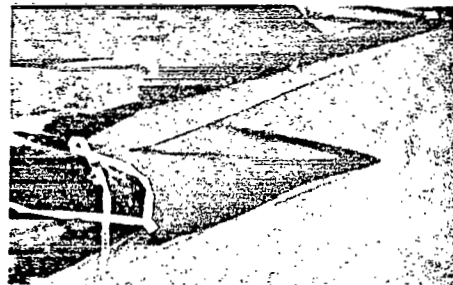
$$R_{x,s} = 13.3 \times 10^6$$



$$R = 145 \times 10^6 / \text{m}$$

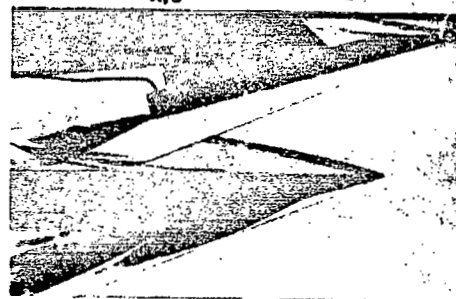
$$R_{x,s} = 25.0 \times 10^6$$

(b) 12.5° wedge generator. L-74-1114



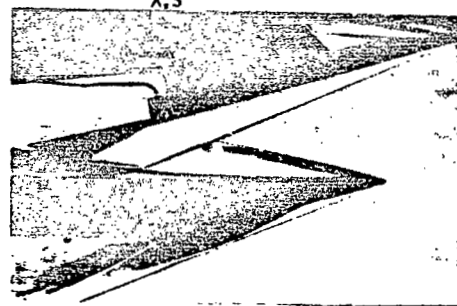
$$R = 36.5 \times 10^6 / \text{m}$$

$$R_{x,s} = 5.85 \times 10^6$$



$$R = 75.9 \times 10^6 / \text{m}$$

$$R_{x,s} = 12.2 \times 10^6$$

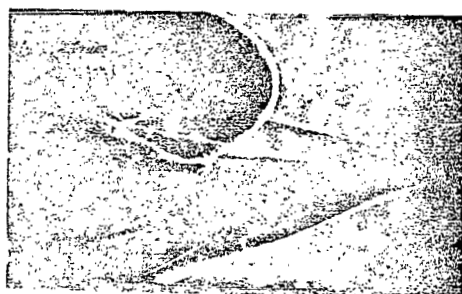


$$R = 149 \times 10^6 / \text{m}$$

$$R_{x,s} = 23.9 \times 10^6$$

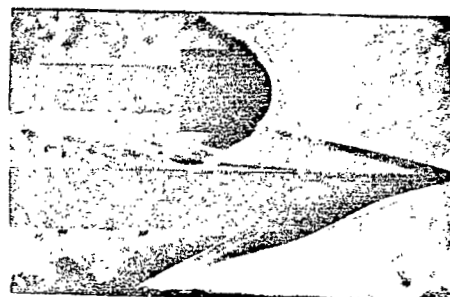
(c) 15° wedge generator. L-74-1115

Figure 7.- Continued.



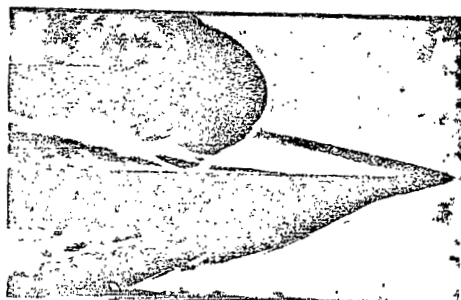
$$R = 8.9 \times 10^6 / \text{m}$$

$$R_{x,s} = 1.38 \times 10^6$$



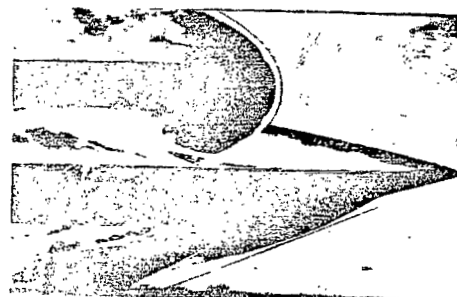
$$R = 18.2 \times 10^6 / \text{m}$$

$$R_{x,s} = 2.82 \times 10^6$$



$$R = 37.5 \times 10^6 / \text{m}$$

$$R_{x,s} = 5.82 \times 10^6$$



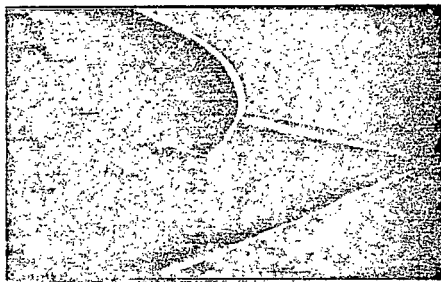
$$R = 74.1 \times 10^6 / \text{m}$$

$$R_{x,s} = 11.5 \times 10^6$$

(c) Sphere generator (2.54 cm above plate).

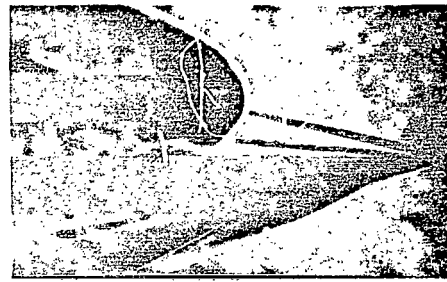
L-74-1116

Figure 7.- Continued.



$$R = 9.8 \times 10^6 / \text{m}$$

$$R_{x,s} = 1.46 \times 10^6$$



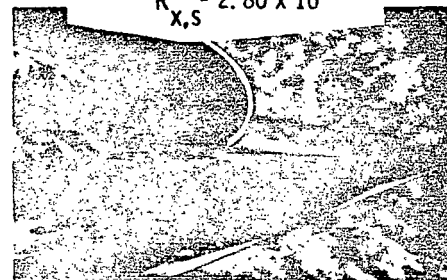
$$R = 18.7 \times 10^6 / \text{m}$$

$$R_{x,s} = 2.80 \times 10^6$$



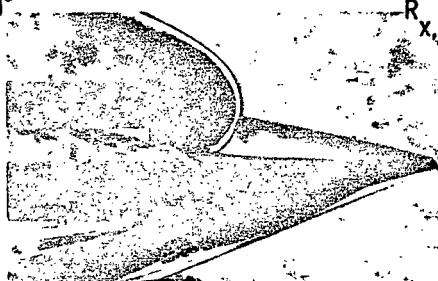
$$R = 36.5 \times 10^6 / \text{m}$$

$$R_{x,s} = 5.46 \times 10^6$$



$$R = 77.4 \times 10^6 / \text{m}$$

$$R_{x,s} = 11.6 \times 10^6$$



$$R = 135 \times 10^6 / \text{m}$$

$$R_{x,s} = 20.2 \times 10^6$$

(e) Sphere generator (1.27 cm above plate).

L-74-1117

Figure 7.- Concluded.

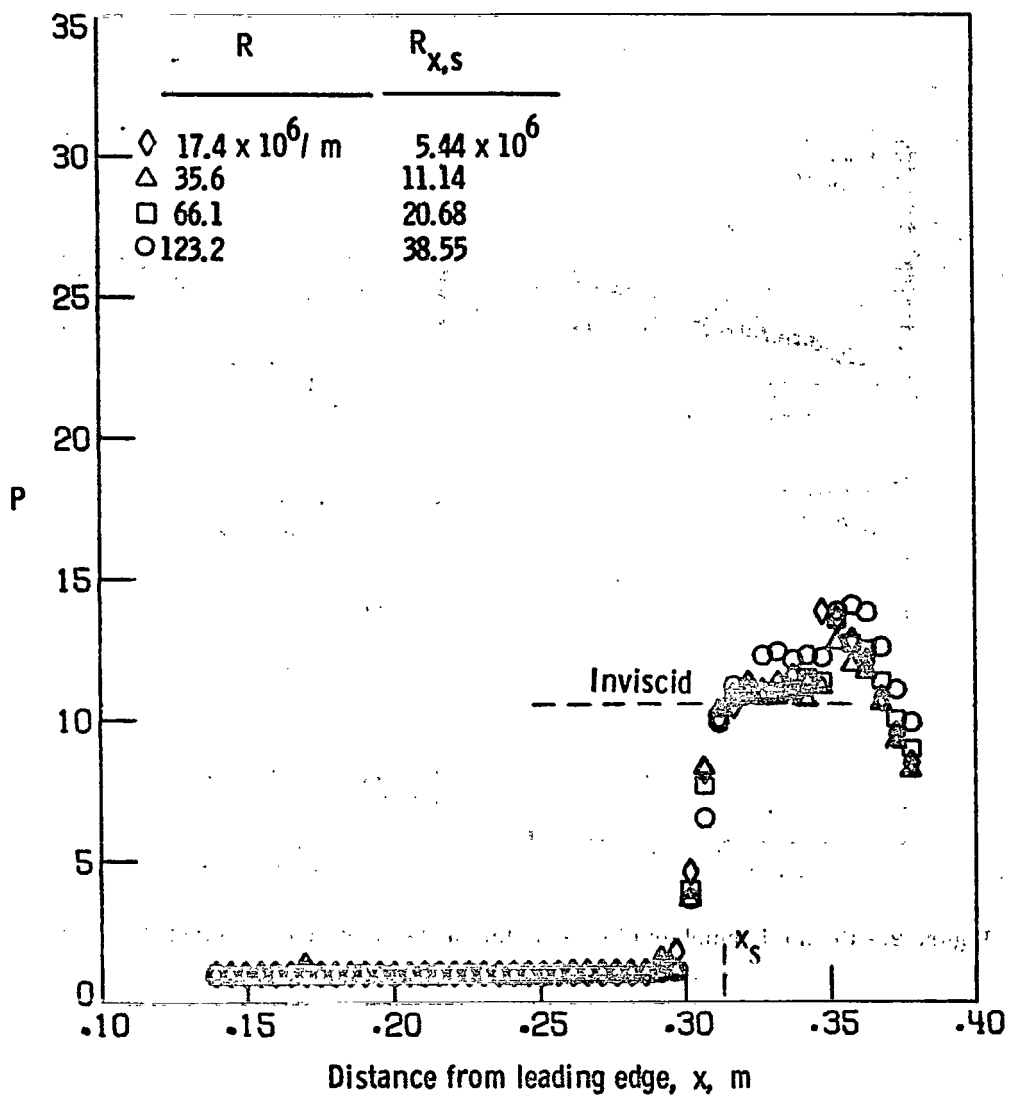


Figure 8.- Interaction pressure ratio distributions on flat-plate, 10° wedge shock generator.

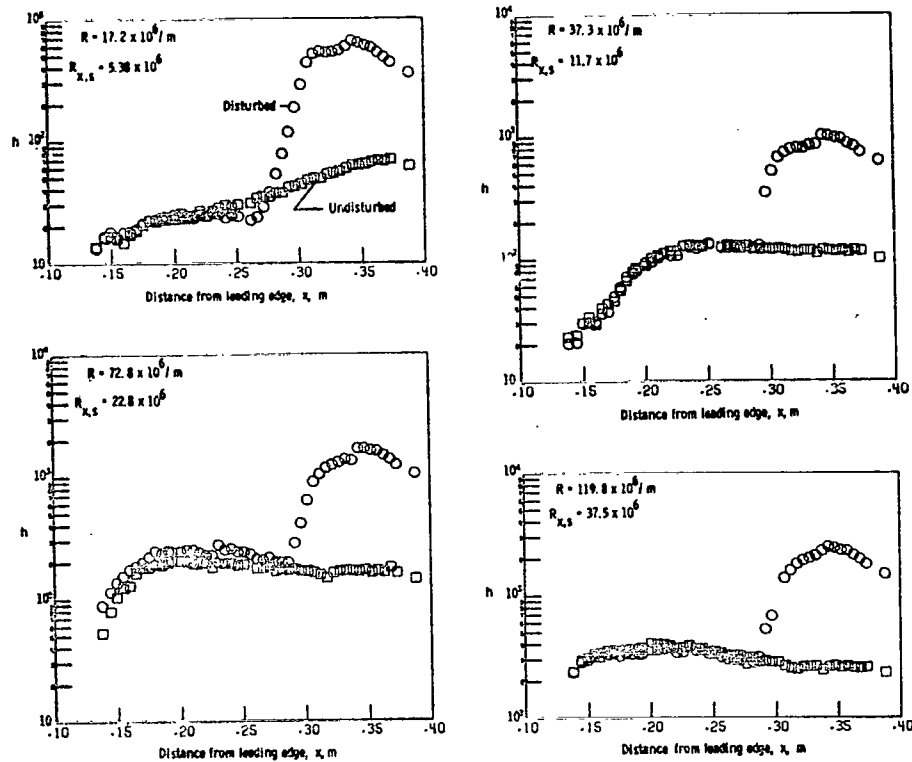


Figure 9.- Reynolds number effects on the heat-transfer coefficient distributions on flat-plate, 10° wedge shock generator.

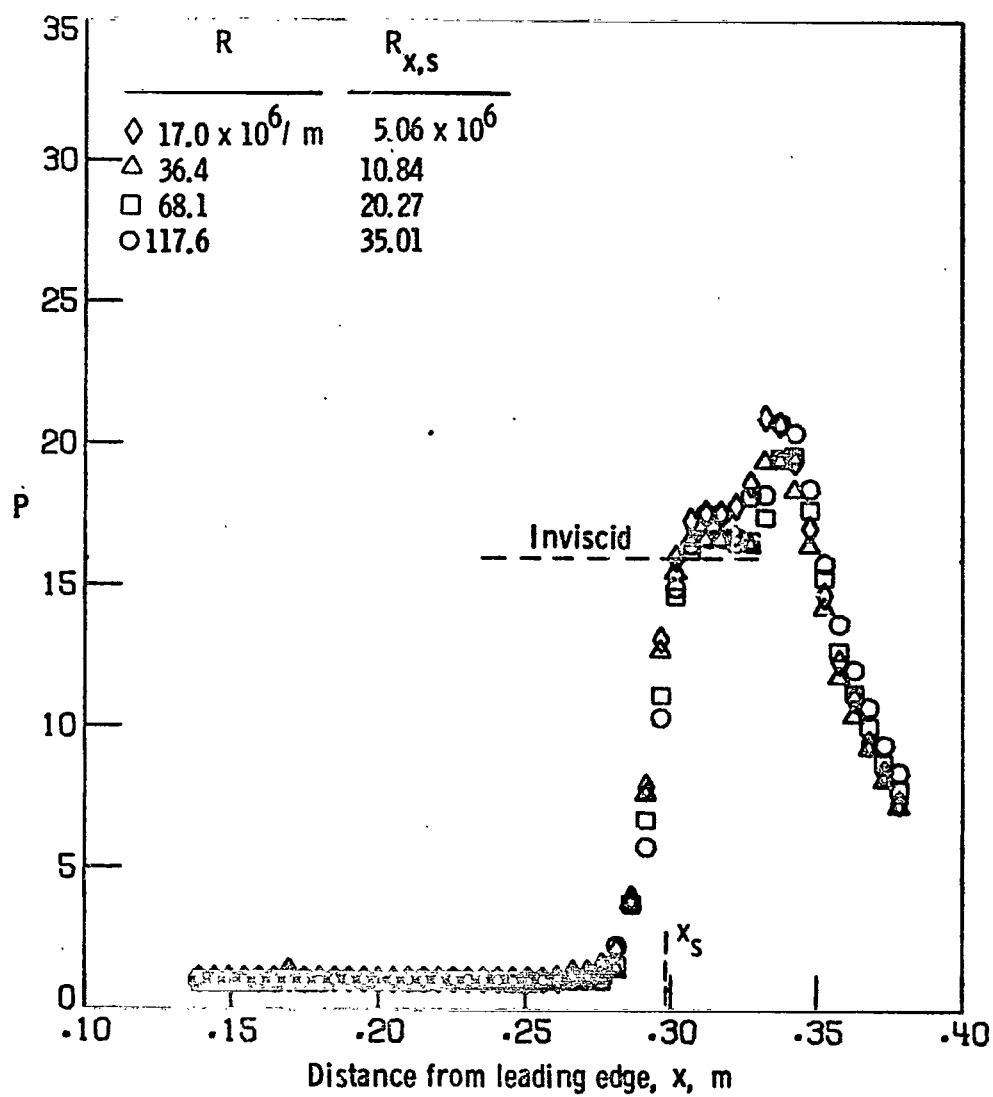


Figure 10.- Interaction pressure ratio distributions on flat-plate, 12.5° wedge shock generator.

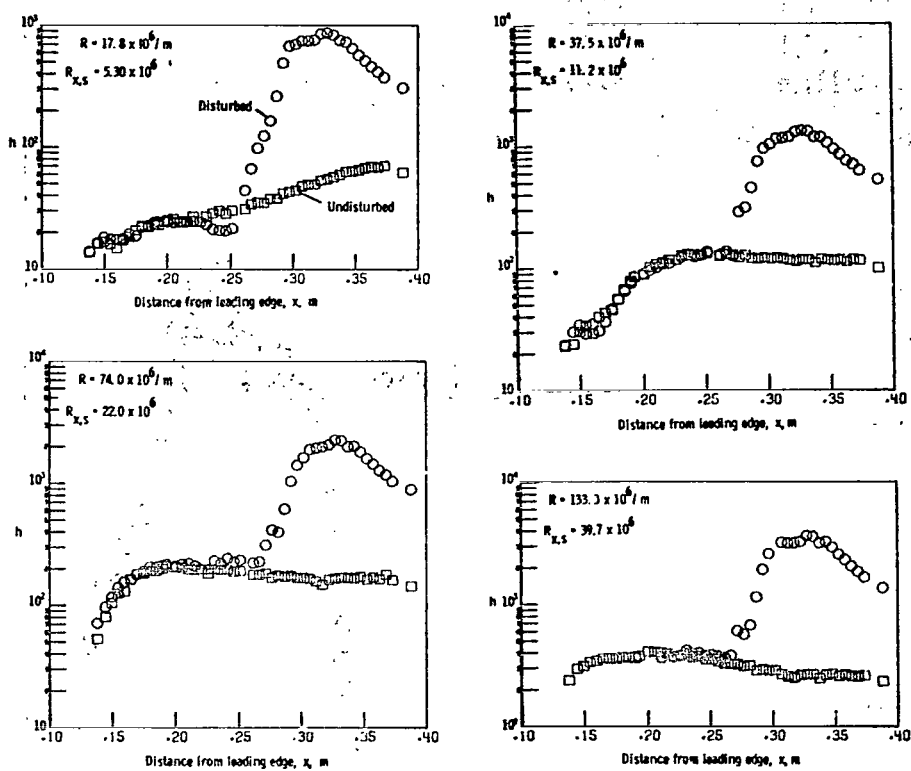


Figure 11.- Reynolds number effects on the heat-transfer coefficient distributions on flat-plate, 13.5° wedge shock generator.

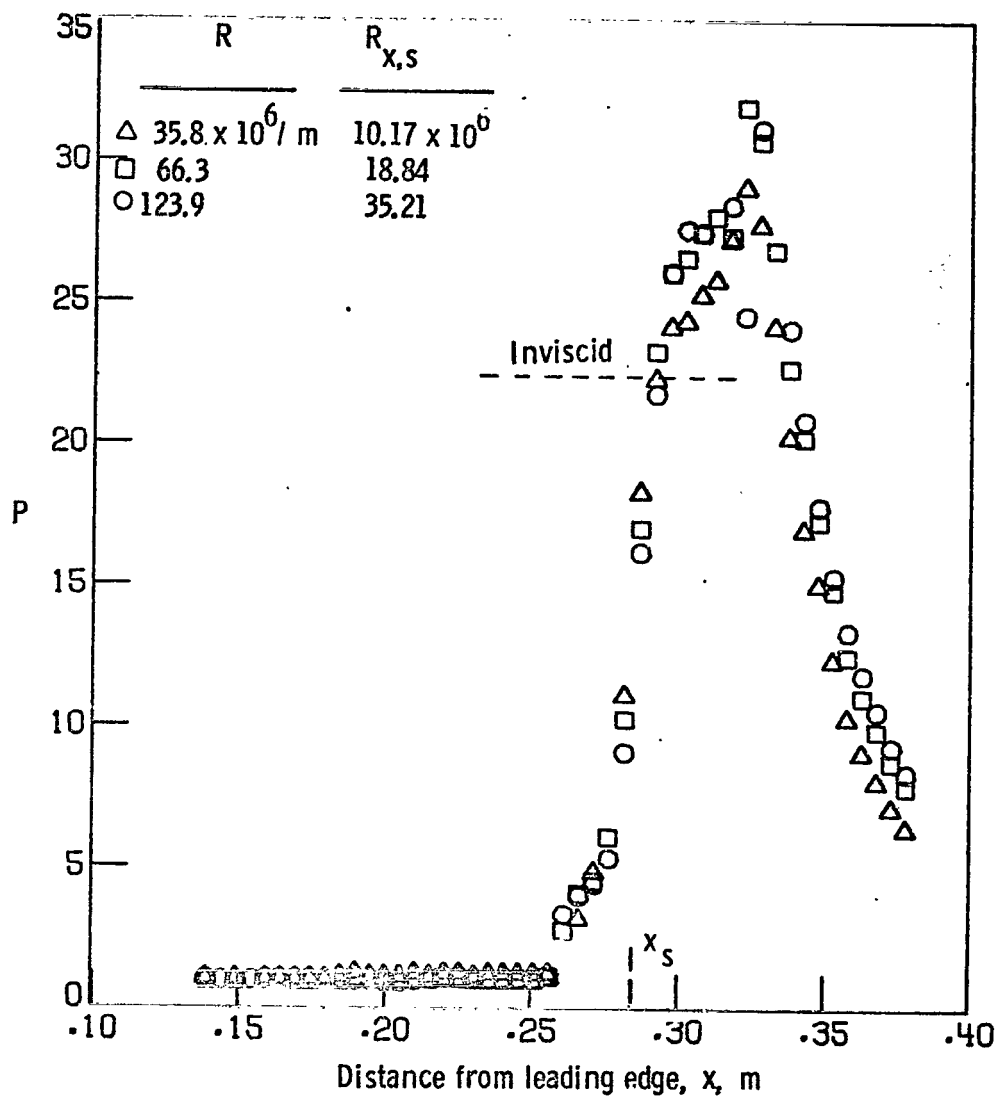


Figure 12.- Interaction pressure ratio distributions on flat-plate, 15° wedge shock generator.

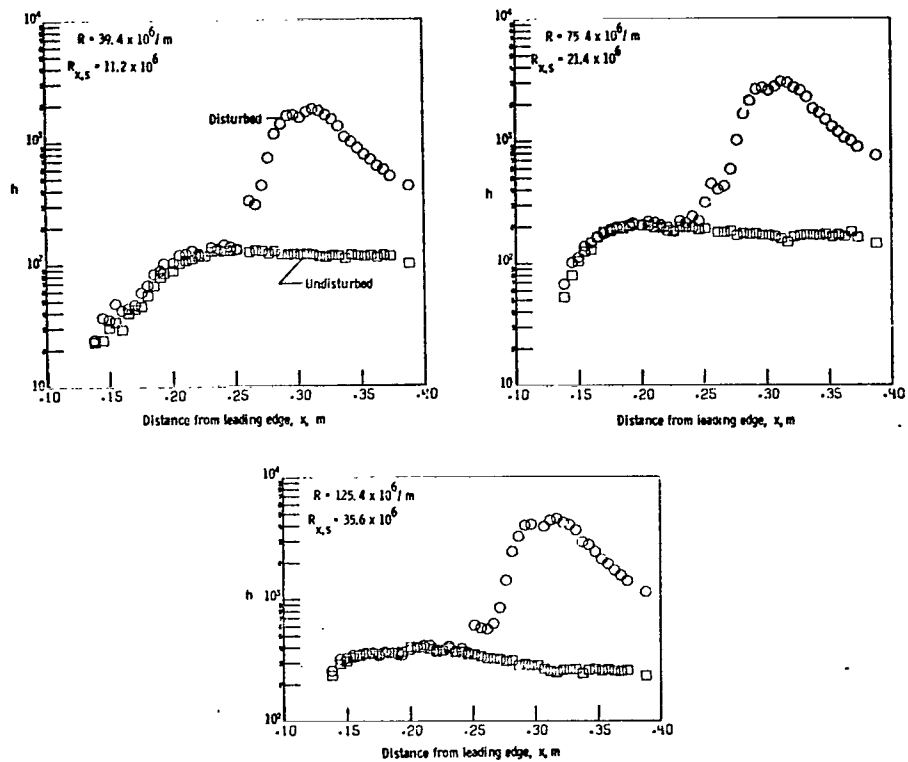


Figure 13. - Reynolds number effects on the heat-transfer coefficient distributions on flat-plate, 15° wedge shock generator.

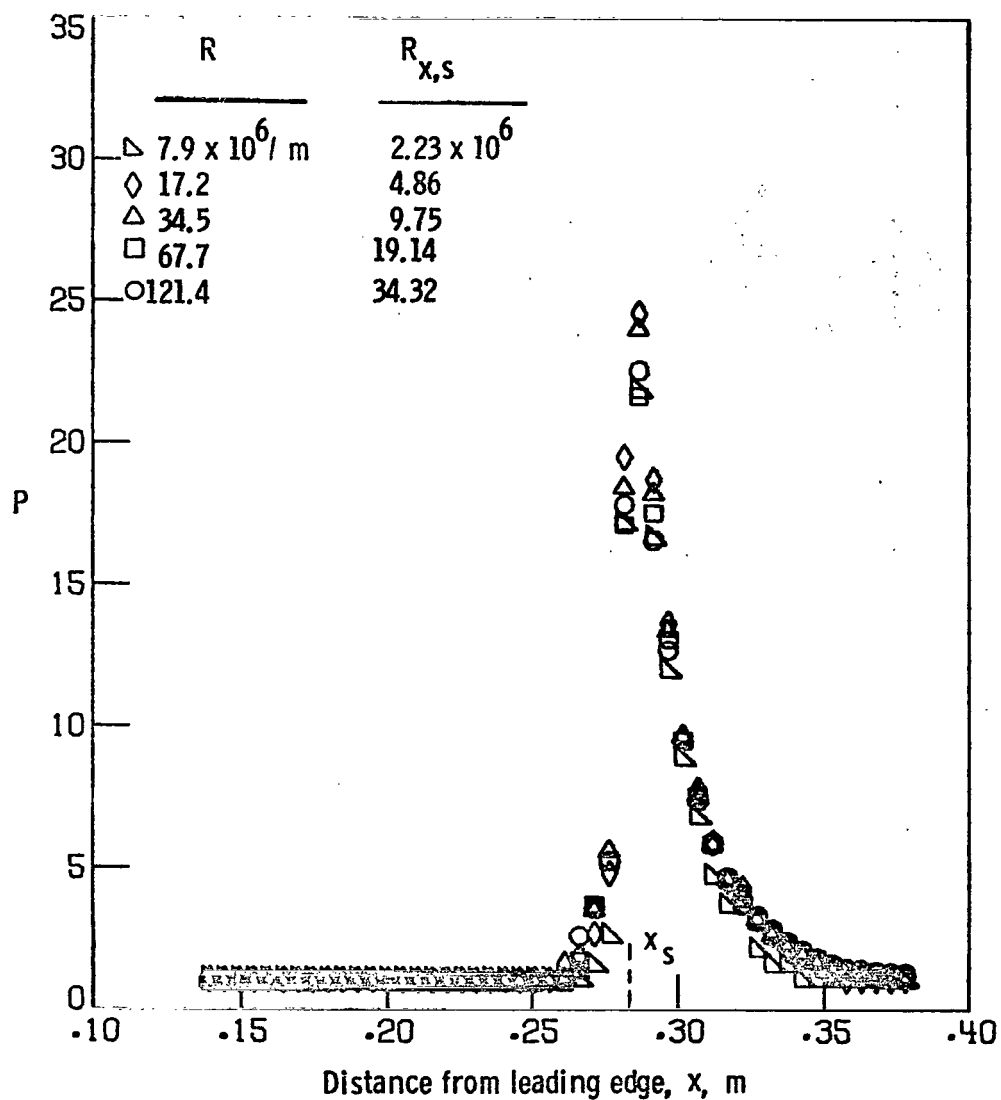


Figure 14.- Interaction pressure ratio distributions on flat-plate, spherical-shock generator, $a_s = 2.54$ cm.

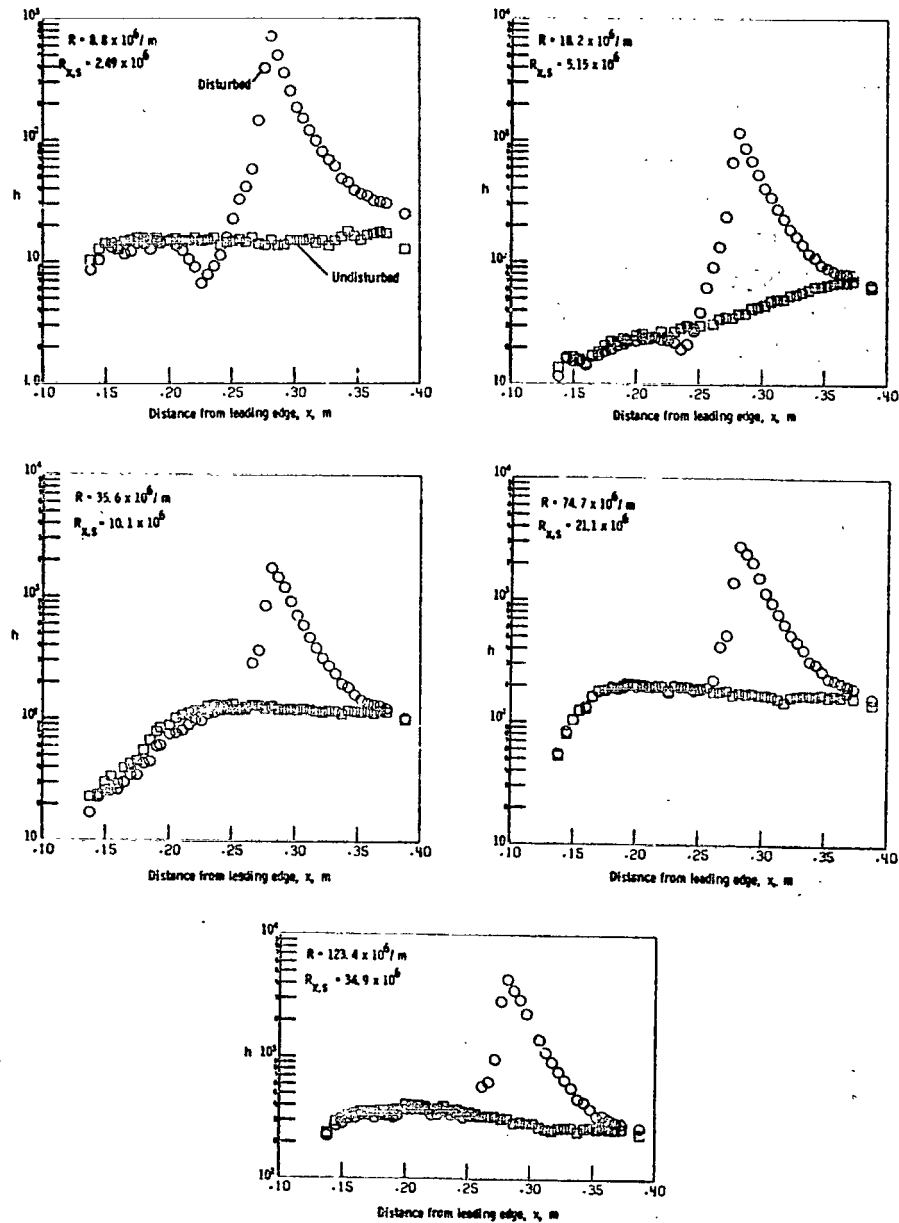


Figure 15.- Reynolds number effects on the heat-transfer coefficient distributions on flat plate, spherical-shock generator, $a_g = 2.54$ cm.

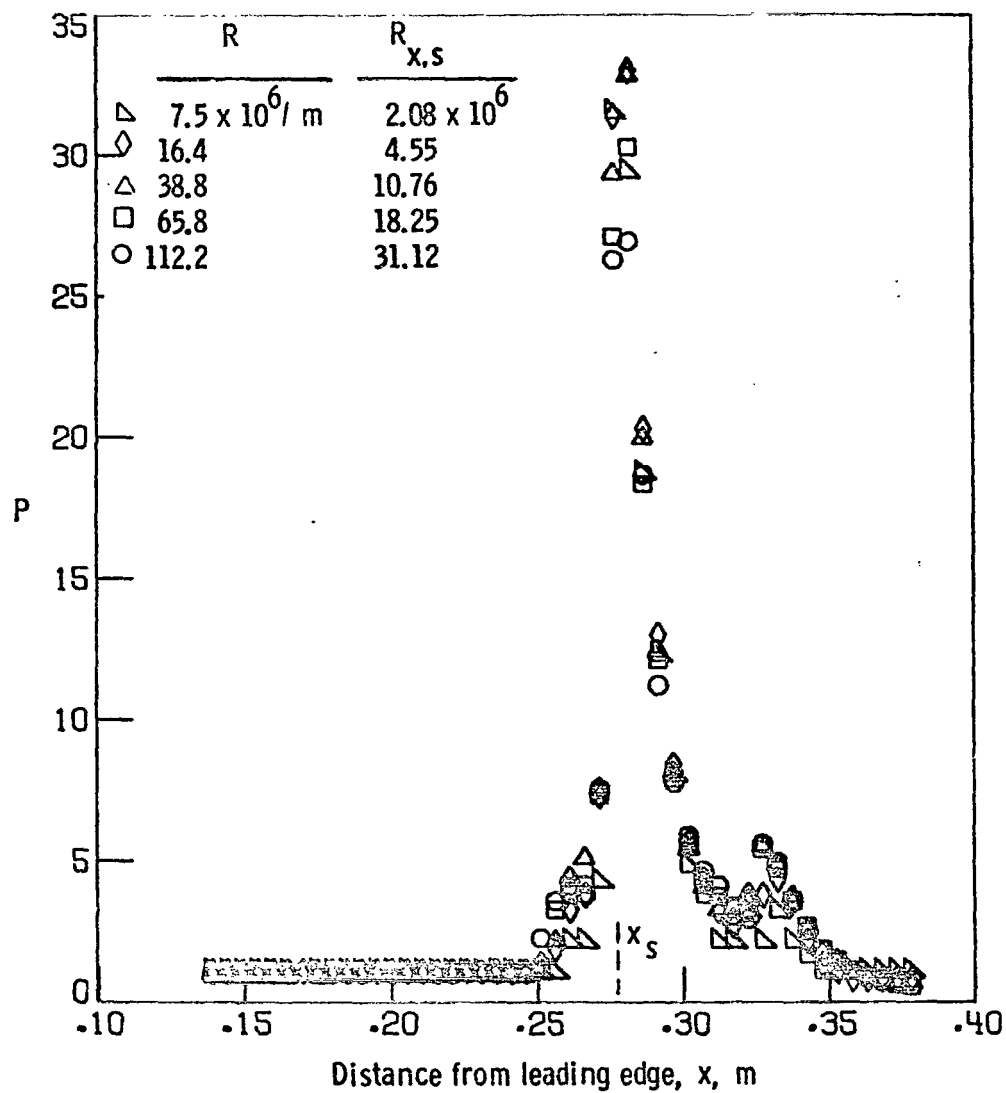


Figure 16.- Interaction pressure ratio distributions on flat-plate, spherical-shock generator, $a_s = 1.27$ cm.

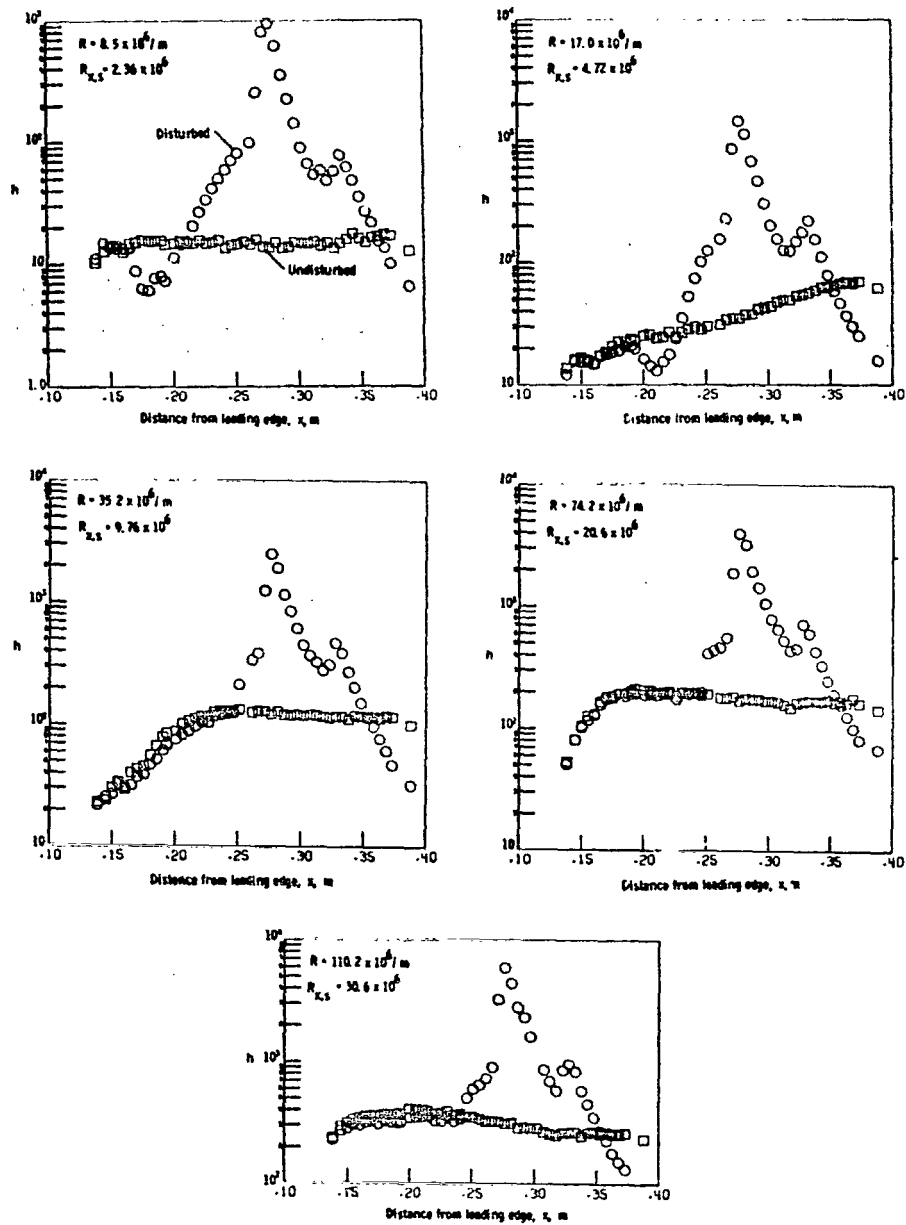


Figure 17.- Reynolds number effects on the heat-transfer coefficient distributions on flat-plate, spherical-shock generator, $a_g = 1.27$ cm.

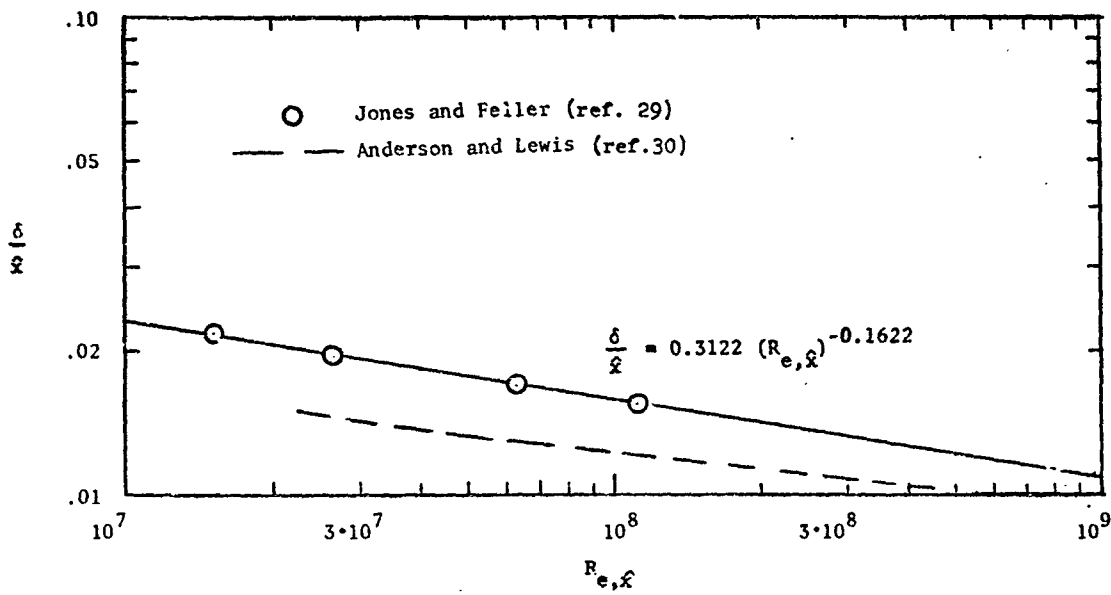


Figure 18.- Tunnel wall boundary-layer thickness for the Mach 6 high Reynolds number facility.

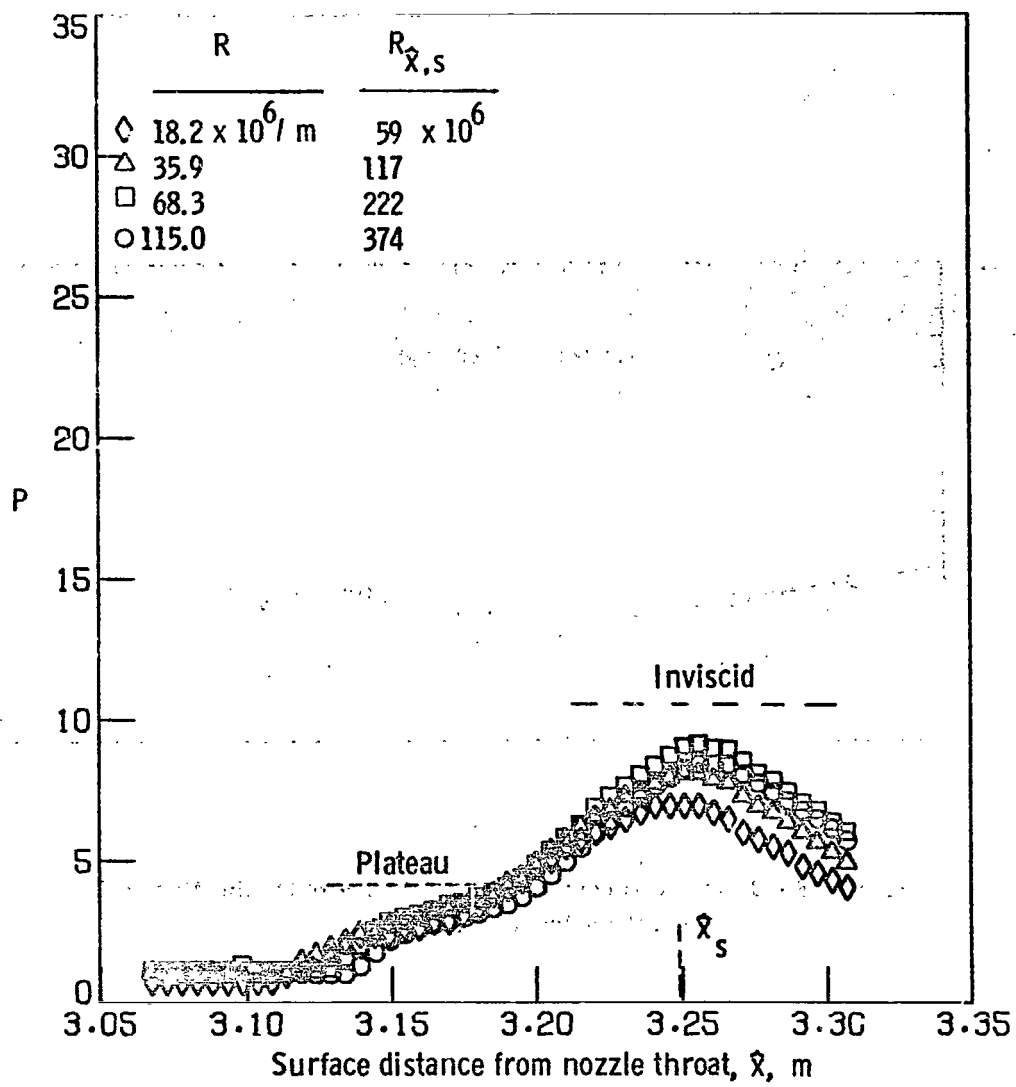


Figure 19.- Interaction pressure ratio distributions on tunnel wall, 10° wedge shock generator.

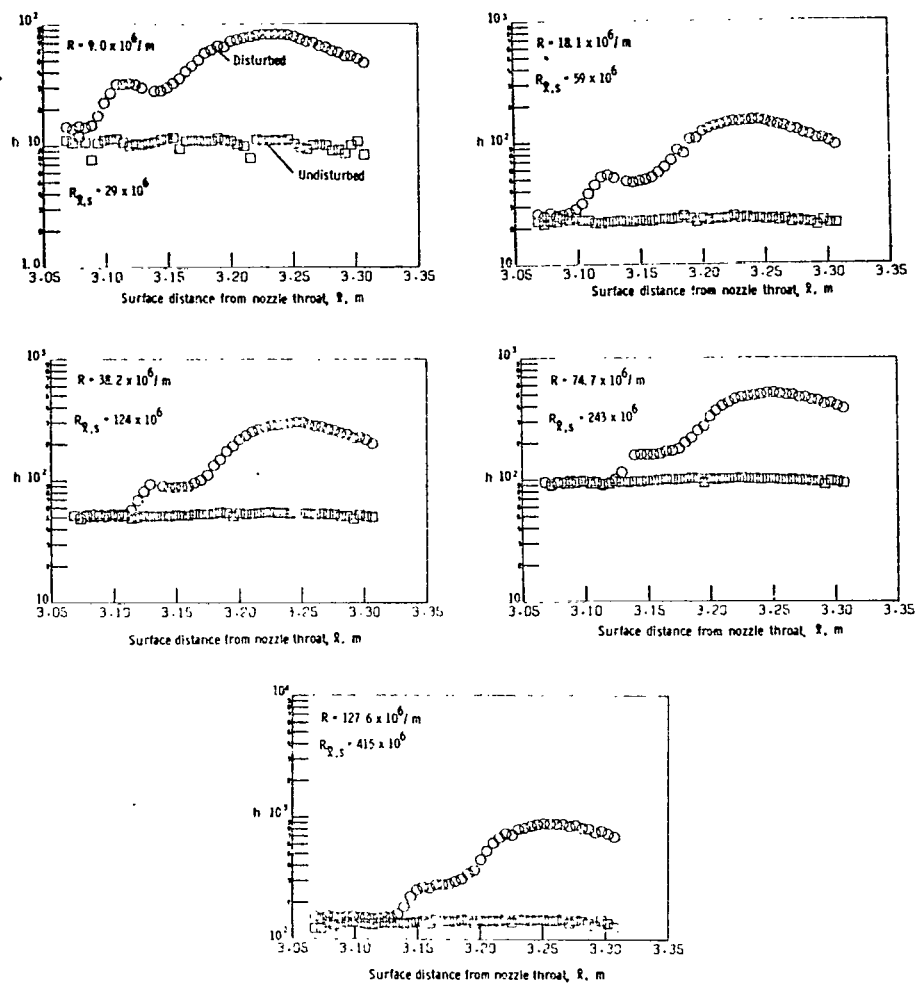


Figure 20.- Reynolds number effects on the heat-transfer coefficient distributions on the tunnel wall, 10° wedge shock generator.

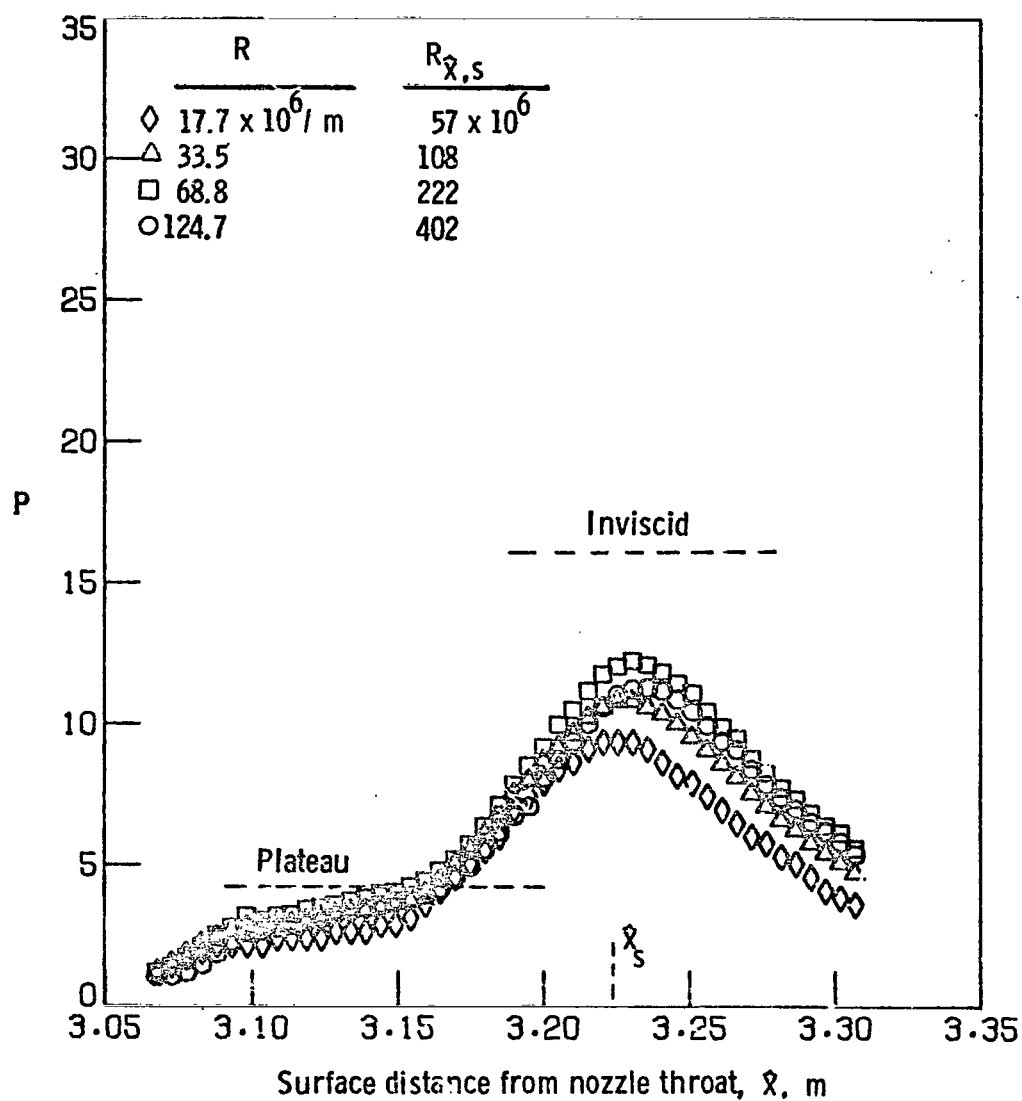


Figure 21.- Interaction pressure ratio distributions on tunnel wall, 12.5° wedge shock generator.

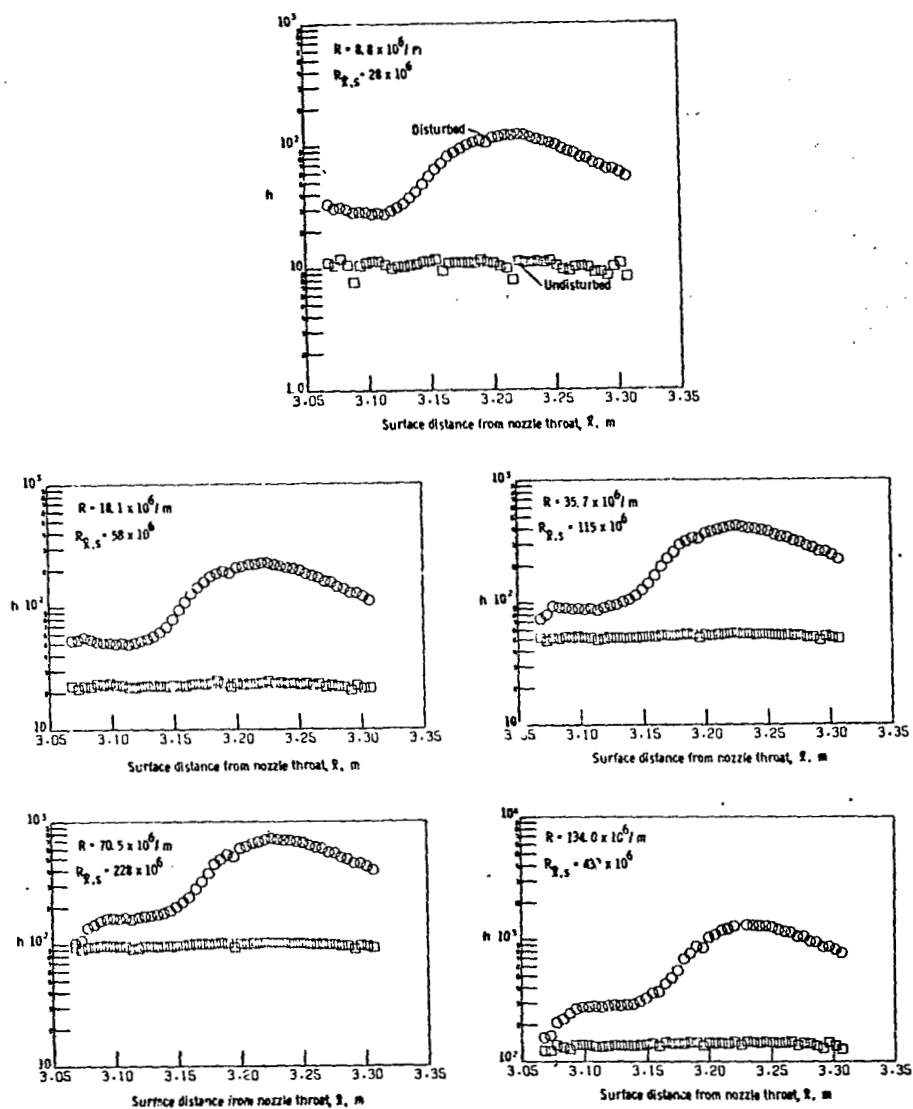


Figure 22.- Reynolds number effects on the heat-transfer coefficient distributions on the tunnel wall, 12.5° wedge shock generator.

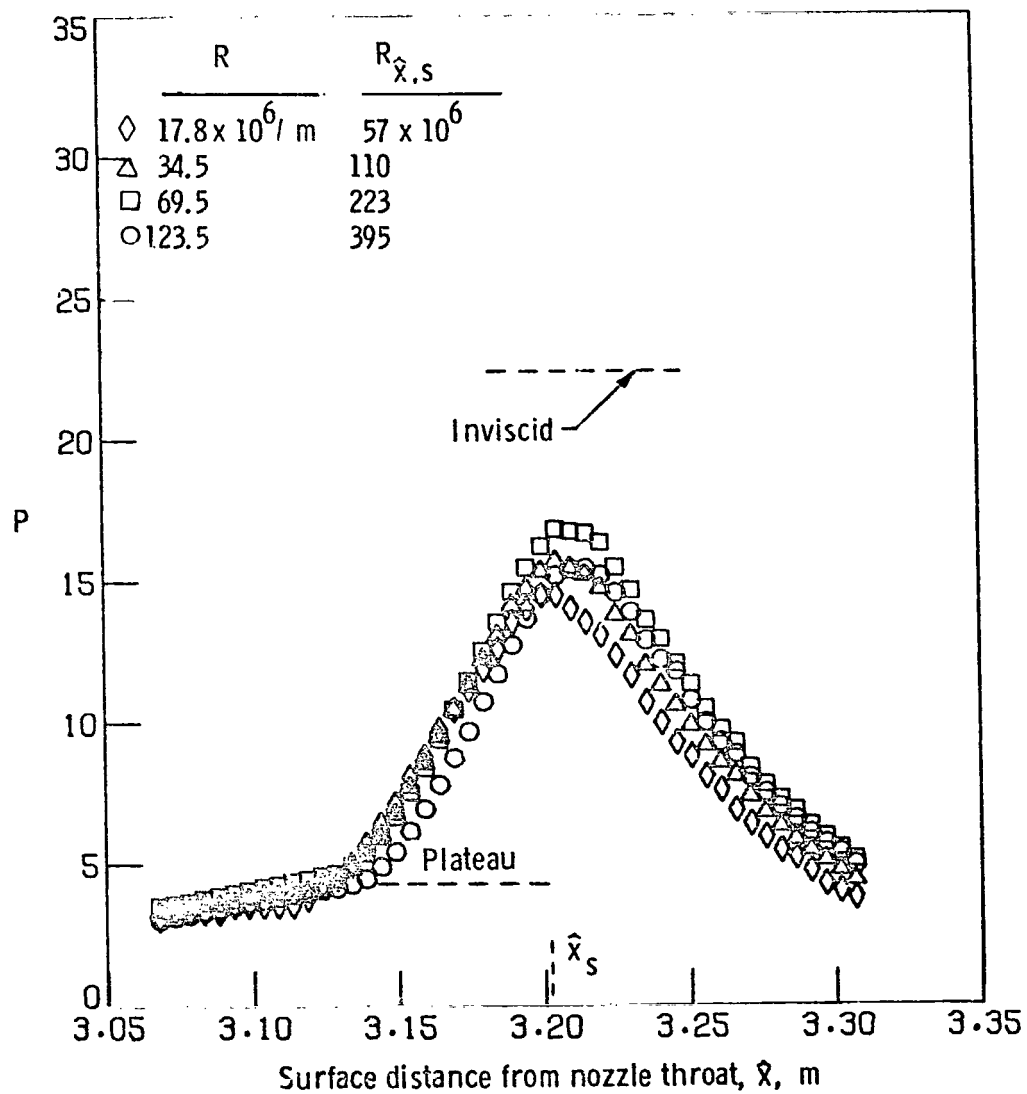


Figure 23.- Interaction pressure ratio distributions on tunnel wall, 15° wedge shock generator.

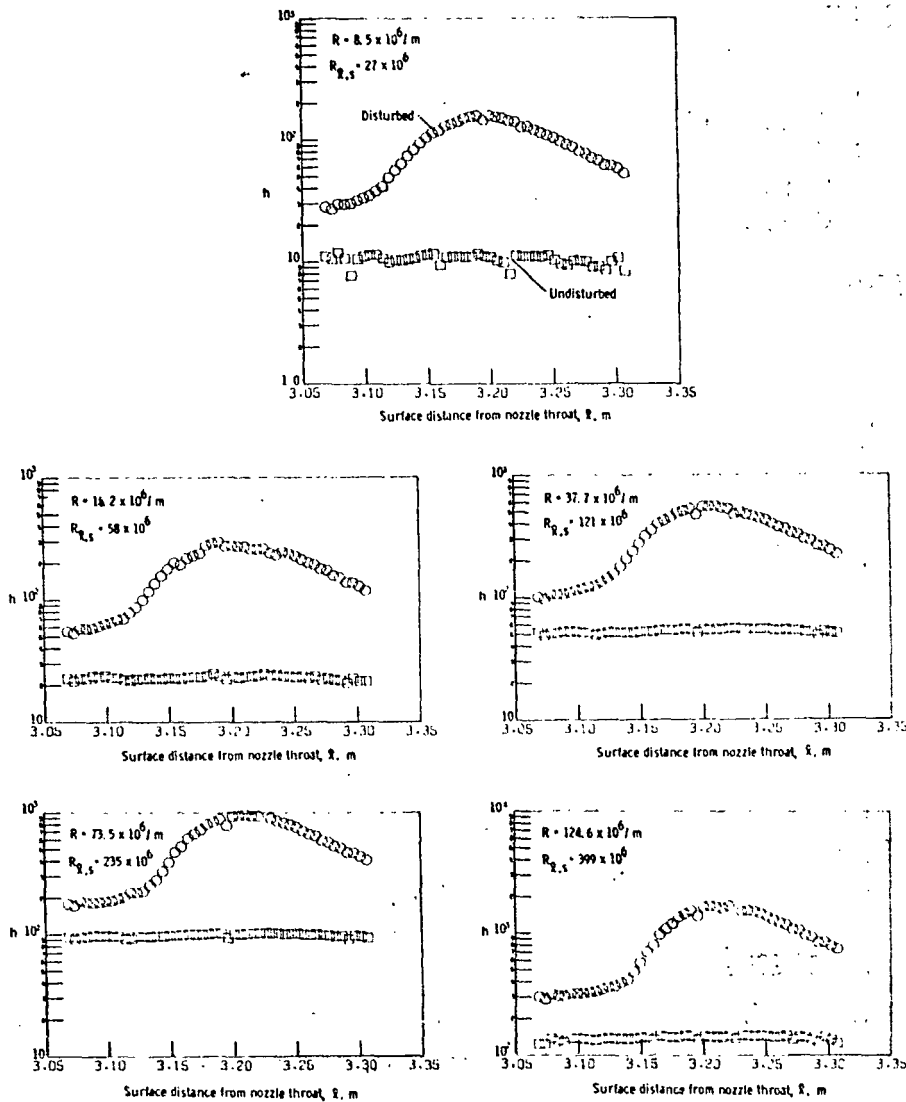


Figure 24.- Reynolds number effects on the heat-transfer coefficient distributions on the tunnel wall, 15° wedge shock generator.

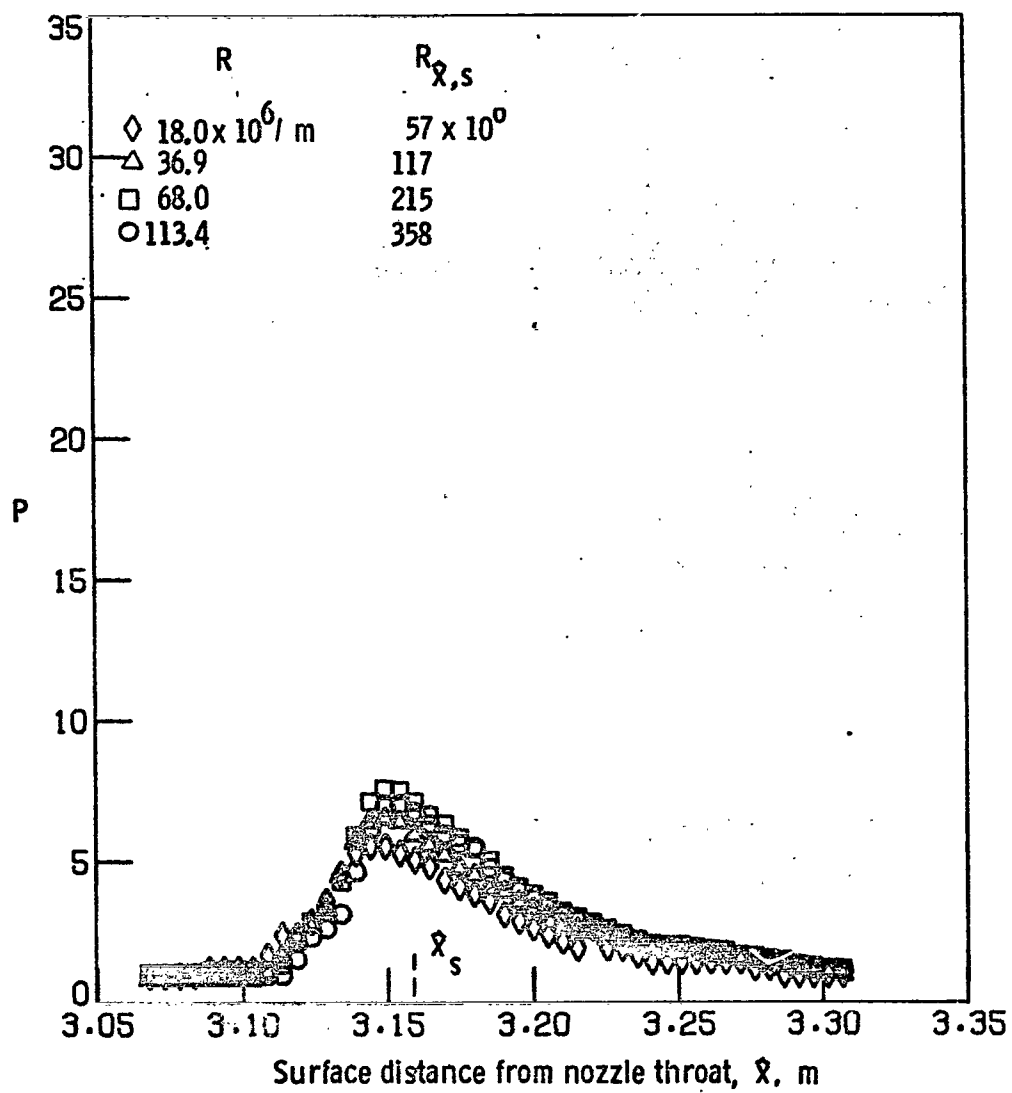


Figure 25.- Interaction pressure ratio distributions on tunnel wall, spherical-shock generator, $\hat{a}_s = 5.08$ cm.

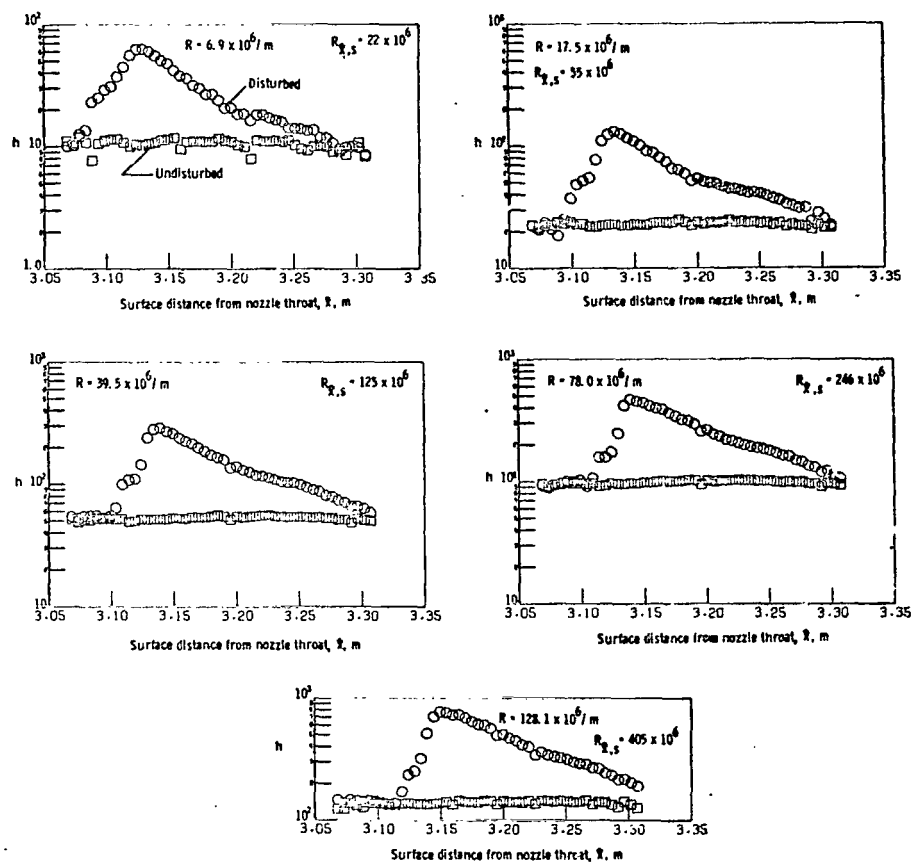


Figure 26.- Reynolds number effects on the heat-transfer coefficient distributions on the tunnel wall, spherical-shock generator, $\hat{a}_g = 5.08$ cm.

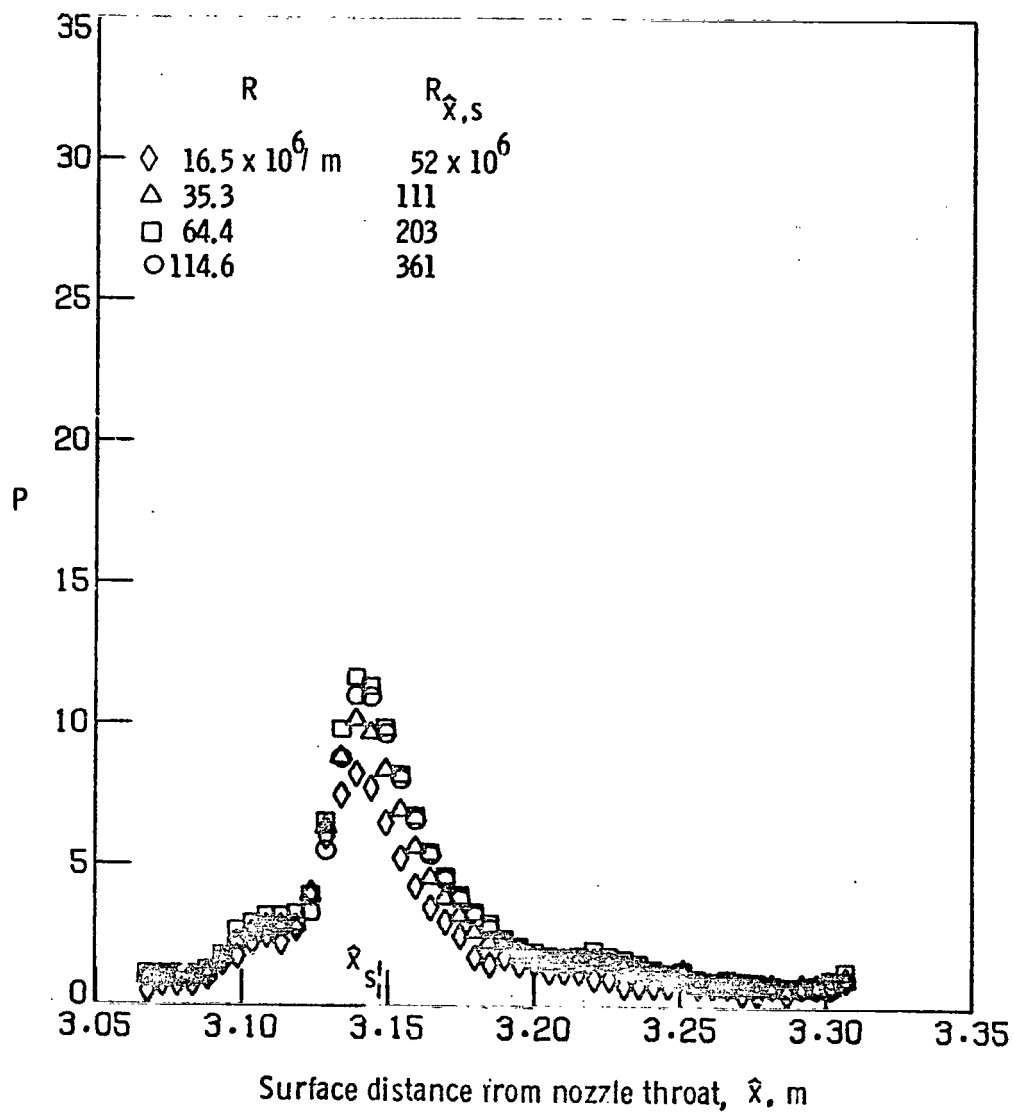


Figure 27.- Interaction pressure ratio distributions on tunnel wall, spherical-shock generator, $\hat{a}_s = 2.54 \text{ cm}$.

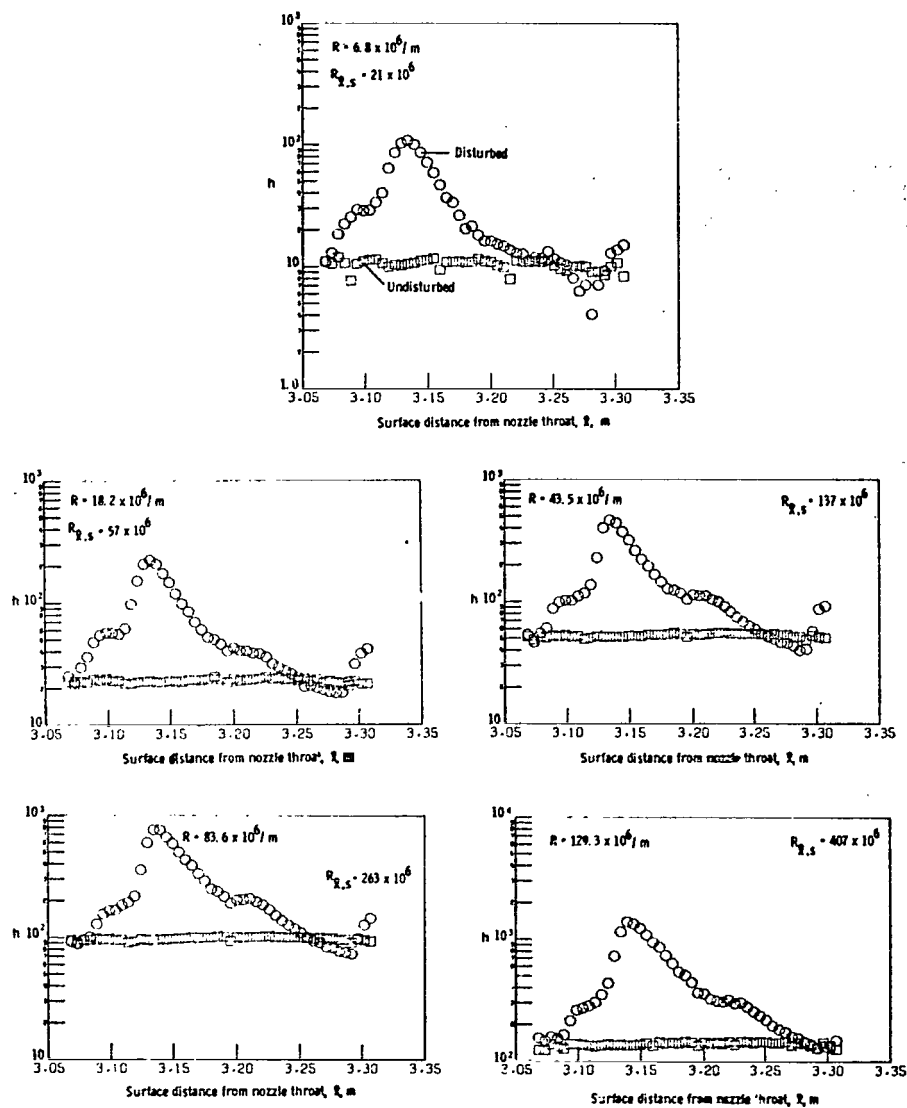


Figure 28.- Reynolds number effects on the heat-transfer coefficient distributions on the tunnel wall, spherical-shock generator, $\hat{a}_g = 2.54$ cm.

θ_w, deg	\circ	12.5 \square	\triangle	\diamond	10 \times	$+$
R	$125 \times 10^6/\text{m}$	$68.8 \times 10^6/\text{m}$	$33.5 \times 10^6/\text{m}$	$115 \times 10^6/\text{m}$	$68.3 \times 10^6/\text{m}$	$35.9 \times 10^6/\text{m}$
\hat{x}_o, m	3.073	3.063	3.063	3.134	3.124	3.119
$R_{\hat{x}_o}$	384×10^6	211×10^6	103×10^6	360×10^6	213×10^6	112×10^6

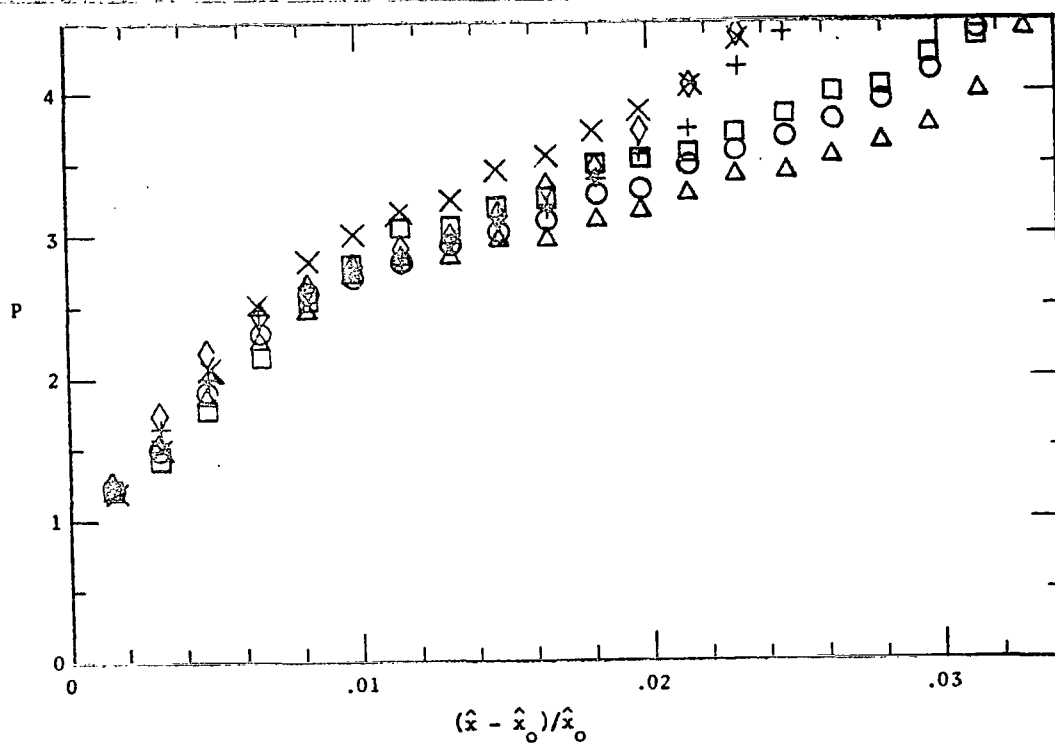


Figure 29.- Initial portion of interaction pressure ratio rises on tunnel wall.

θ_w, deg	12.5			10		
γ	○	□	△	◇	×	+
\hat{x}_o, m	$125 \times 10^6/\text{m}$	$68.8 \times 10^6/\text{m}$	$33.5 \times 10^6/\text{m}$	$115 \times 10^6/\text{m}$	68.3×10^6	$35.9 \times 10^6/\text{m}$
$R_{\hat{x},o}$	3.073	3.063	3.063	3.134	3.124	3.119
	384×10^6	211×10^6	103×10^6	360×10^6	213×10^6	112×10^6

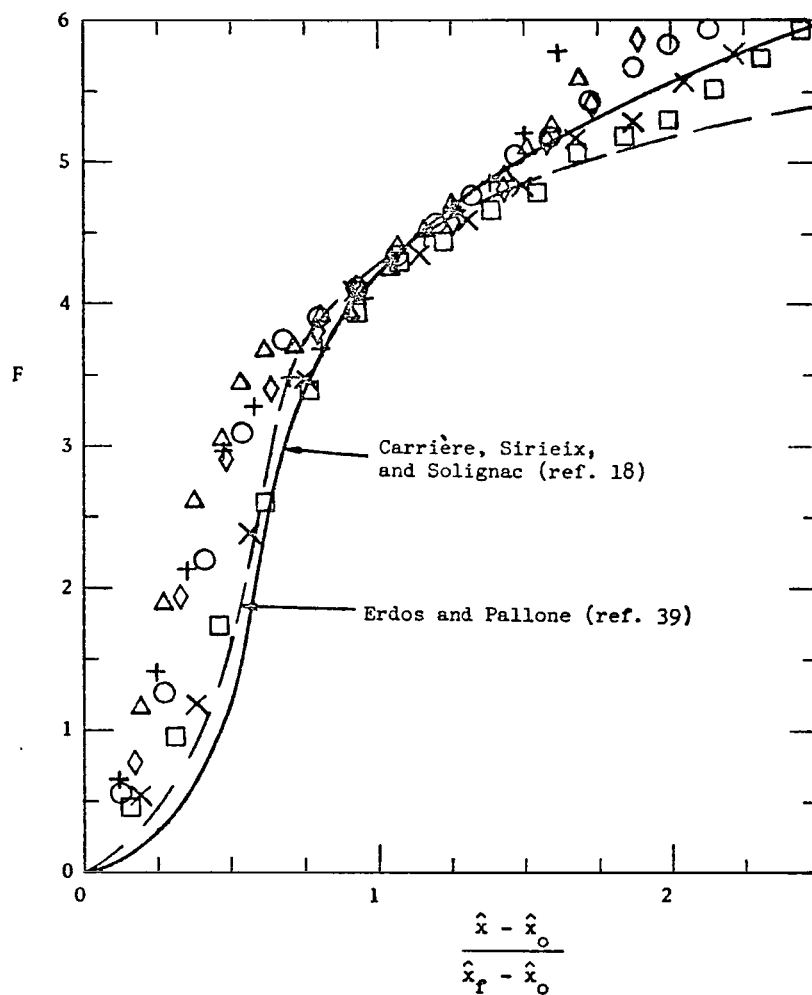


Figure 30.- Turbulent free interaction pressure rises on tunnel wall
(F defined in eq. (8)).

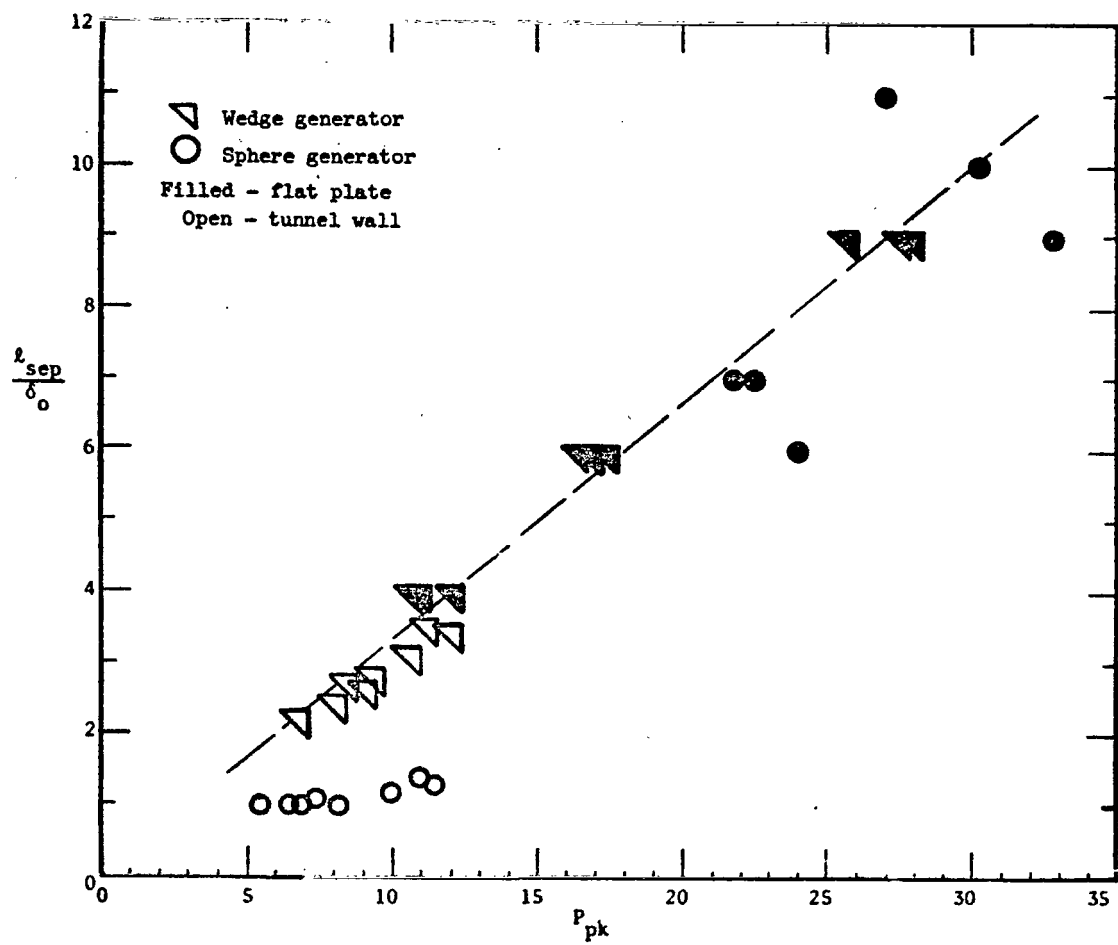


Figure 31.- Separation lengths versus peak pressure rise ratios.

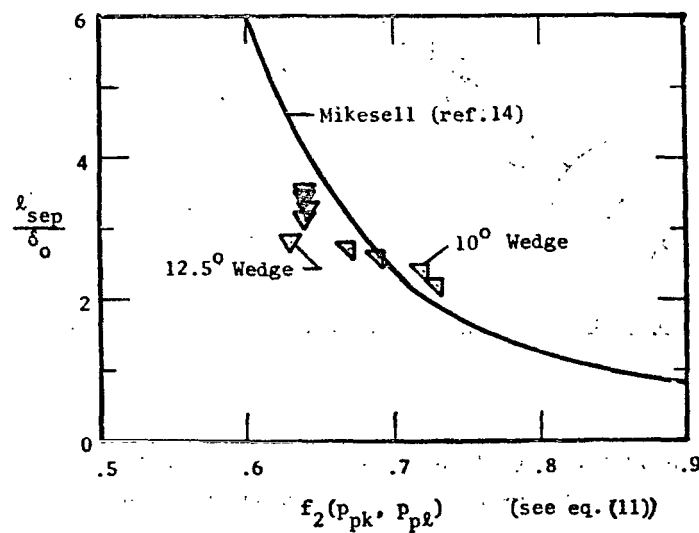
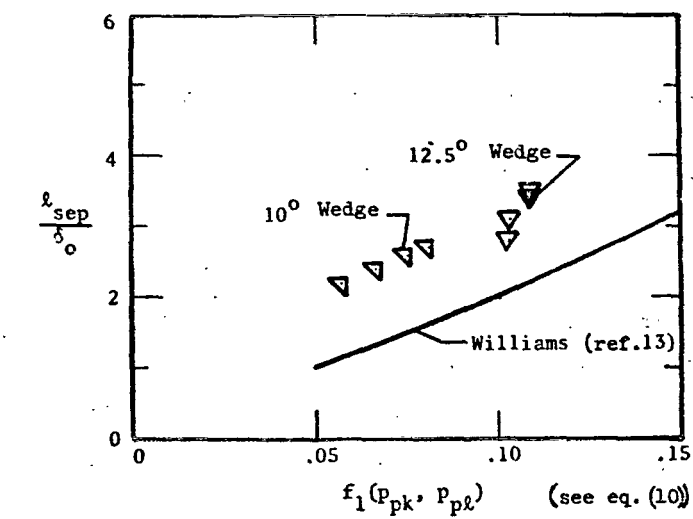


Figure 32.- Separation length as functions of parameters suggested by Williams (ref. 13) and by Mikesell (ref. 14).

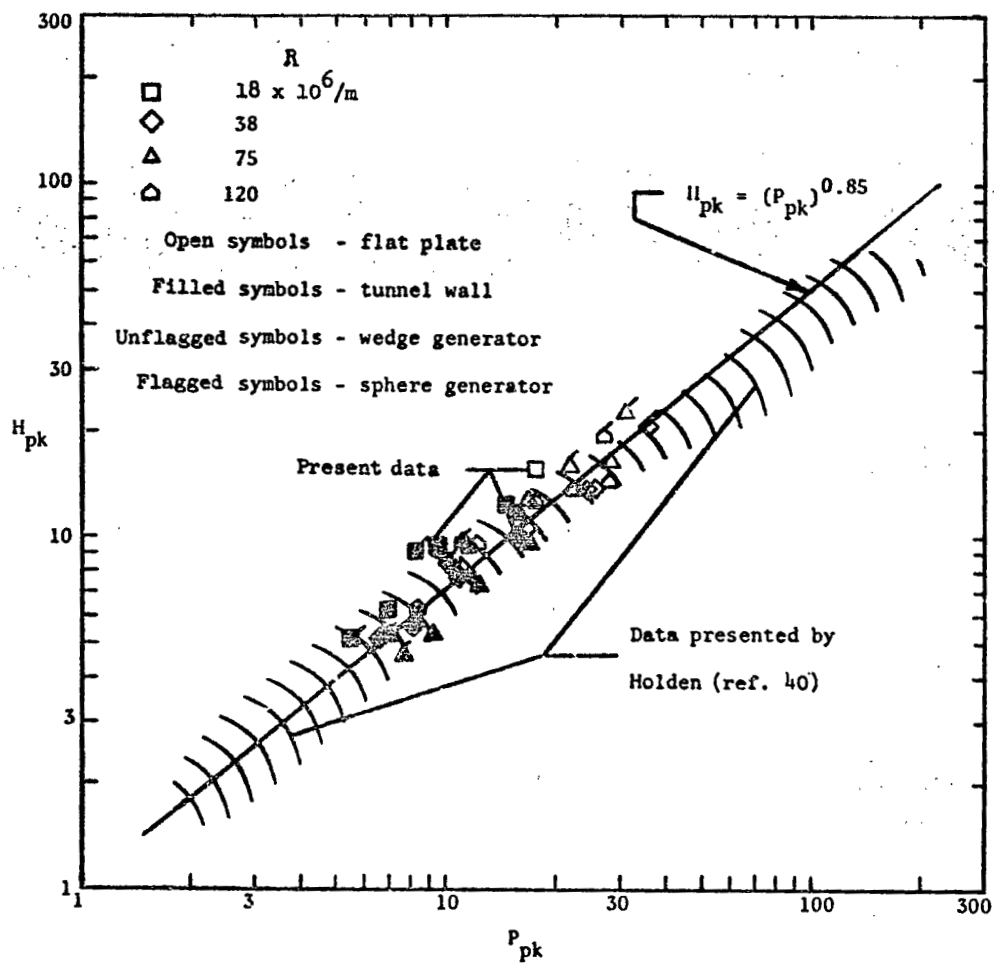


Figure 33.- Correlation of peak-heating-rate amplifications with peak-pressure-rise ratios for fully turbulent boundary layers.

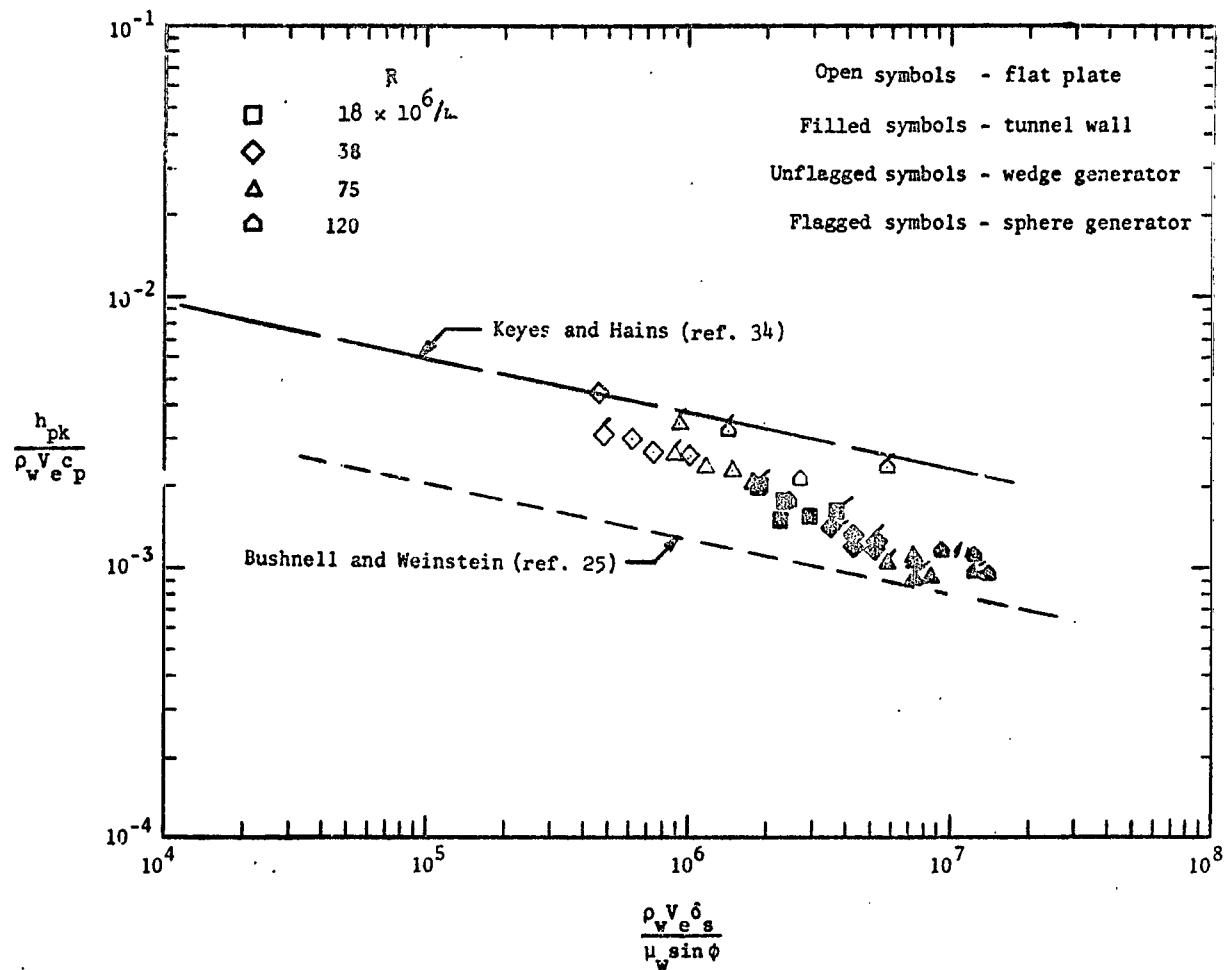


Figure 34.- Correlation of peak heating at reattachment for fully turbulent boundary layers, using parameters suggested by Bushnell and Weinstein (ref. 25).

END

DATE

FILMED

OCT 17 1974